Production Cross Sections of neutron-deficient isotopes in ^{36}Ar at 1050 A·MeV + ^{9}Be collisions

Manuel Caamaño Fresco

Junio 2002

Contents

List of Figures

List of Tables

Introduction

Since the pioneering experiments at Berkeley [1][2], projectile fragmentation has been widely used to produce radioactive isotopes far from stability. The recent production of secondary beams has enlarged the field of nuclear physic studies making possible experiments involving exotic species. The measurement of production cross sections will figure among the first experiments to be performed with those secondary beams. This kind of experiments will provide important information to plan other experiments involving these exotic beams (estimations of the needed time for the experiment), at the same time that can be used to extract information about the reaction mechanism.

The production cross section (σ_p) is the probability of producing certain isotope from a certain reaction in units of area. Experimentally, with thin targets, can be defined as the number of produced particles (N_p) divided by the number of incident particles (N_i) and the number of atoms in the target in units of area (T_f):

$$\sigma_p = \frac{N_p}{N_i \cdot T_f} \tag{1}$$

The optimal situation would correspond to the case where any production cross section has been measured in the laboratory. This situation is unrealistic due to the large number of exotic isotopes that can be produced. However it is very important to perform these measurements all over the nuclide chart to build a data base that can be used to optimize theoretical models to predict these quantities.

These quantities are difficult to evaluate with physical projectile-fragmentation models, such as the Abrasion-Ablation model [3] or the intra nuclear cascade used in ISABEL code [4][5]. The main problem related to this kind of models is that the calculations that they involve are time consuming. Under this perspective it is very important to develop parameterizations able to estimate those quantities. Using an empirical parametrization one can be confident that the predictions will be closer to the experimental results. The degree of precision of these parameterizations depends on the quality and amount of the experimental data that are taken into account. One of these approaches is the so-called EPAX formula [6][7].

In this work we measure the production cross section (σ_p) for a certain number of neutron-deficient isotopes, from Ar to N, in a $^{36}Ar+^{9}Be$ fragmentation reaction at 1050 $A \cdot MeV$. The experiment was performed at the SIS/FRS facility [9] of GSI in Darmstadt, Germany. We obtain neutron-deficient fragmentation residues, reaching the proton drip line in some cases.

This work starts with a brief introduction to the production of radioactive beams,

the methods and the main fields of study. The projectile fragmentation method used in the present experiment is included with some introducting concepts useful to follow the rest of the work.

In chapter 2 we describe the SIS/FRS facility, at GSI, where the experiment took place. The description of the FRS spectrometer, and the different settings in which was used is also included, as well as some details about the detectors used.

The data analysis is presented in chapter 3. The procedure to obtain the three quantities (the number of produced particles (N_p), the number of incident particles (N_i) and the number of atoms in the target per units of area (T_f)) needed to calculate the production cross section (σ_p) for all the isotopes identified is described in first place. Then we explain the corrections applied in order to get the final values. And finally, we describre the sources of the uncertainties in the whole calculation for the final results.

The results are presented in chapter 4. They are compared with the theoretical predictions of the Abrasion-Ablation, and intra nuclear cascade models and the semi-empirical parametrization EPAX. These results will be part of the data base of EPAX in a further attempt to improve their predictions. The momentum distributions of the isotopes will also be presented and compared with the Morrissey [10] and Goldhaber [11] models at the end of this chapter.

The conclusions and perspectives of this work are presented in chapter 5.

Chapter 1

Production and Use of Radioactive Beams

For a long time the research field of nuclear physics was limited by the only use of stable nuclei. The isotopes were produced close to the stability valley, where the ratio N/Z is well balanced, and the reactions to study were constrained to this region too. We can see in fig. 1.1 how these nuclei, marked with black squares, represent a small amount of the known nuclides. The development of radioactive beams allows us to go far from the line of stability and to perform experiments involving nuclei with a non balanced N/Z ratio. The number of possible nuclei and different kinds of reactions has increased considerably, and new regions in the chart of the nuclides, particularly its limits in number of protons and neutrons, the drip lines, have started to be explored.

Two methods are generally used to produce radioactive beams: the projectile fragmentation and the ISOL technique. We give a short explanation about them in the following section, paying special attention to the projectile fragmentation, used in this experiment. The main fields of study opened with these radioactive exotic beams are briefly reviewed at the end of this chapter.

1.1 Methods of Production

We introduce in this section the main production methods of exotic nuclei [12], these are summarize in fig. 1.2:

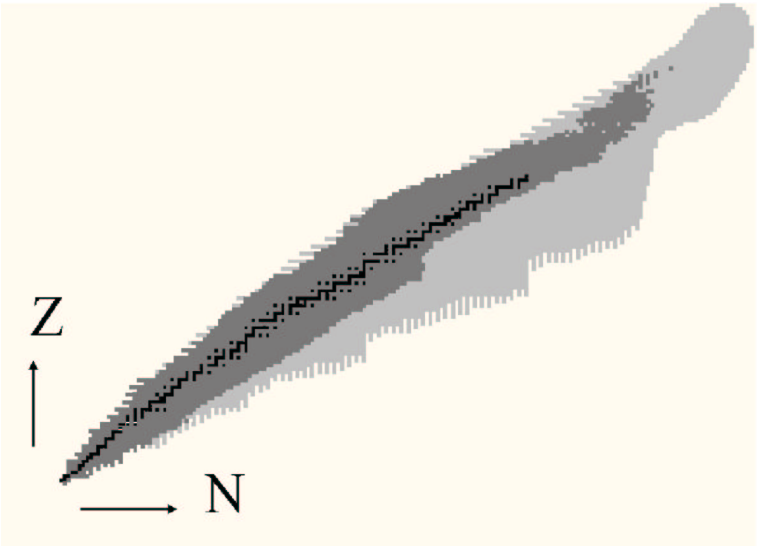

Figure 1.1: *The figure shows the chart of nuclei. The stable nuclei are marked with black squares. The known nuclei cover the dark grey regions. The light regions correspond to theoretical predictions of unknowing bound nuclides.*

- The ISOL method followed by an acceleration of the produced nuclei.
- The in-flight projectile fragmentation.

1.1.1 ISOL Method

To produce secondary beams we can use, in principle, any nuclear reaction giving radioactive products. The Isotope Separation On Line (*ISOL*) gives the chance to use different kinds of reaction to produce radioactive nuclei, such as fragmentation, spallation, or induced fission.

In the ISOL method the radioactive species are produced at rest in a thick target, bombarded with a primary beam coming from a primary source or a driver accelerator. The products are ionized, selected, and extracted from the target by electromagnetic devices. Then these nuclei can be accelerated in a post-accelerator.

This technique produces high intensity and high quality radioactive beams, generally at energies up to 25 MeV/u [12]. The main limitation of the ISOL method comes from the extraction of the products from the target. This process can be difficult and low efficient (dependent on the produced specie). The long time needed for the extraction (seconds in some cases) limits the number of exotic species that can

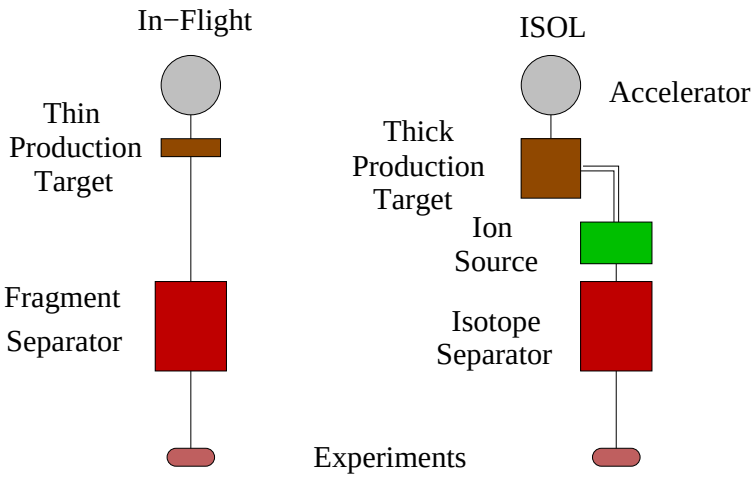

Figure 1.2: *The figure shows the two basic methods to produce radioactive nuclear beams. On the right, the ISOL method is depicted. On the left, the in-flight method.*

be produced due to their lifetime. Production of very unstable nuclei are virtually impossible.

1.1.2 Projectile Fragmentation

Projectile fragmentation is a very powerful method to produce a large number of secondary beams with high energies and intensities.

When a high energy projectile beam impinges in a target, a large number of fragments are produced in a narrow forward cone, with a wide range of N/Z ratio. The projectile fragmentation allows us to explore regions far from the line of stability.

The production cross section related to this process is almost energy independent. Above a certain energy the value of the production cross section is proved to be constant. This hypothesis is based in a high energy physics concept, the *limiting fragmentation* [8], experimentally tested [13] in nuclear fragmentation. It was also found that the momentum distribution of the produced fragments is similar for this energy range and follows a systematic behavior.

The election of the target is an important question in projectile fragmentation. We can suppose that the fragmentation cross section depends on the mass of the target as $\sigma_{frag} \propto A_{targ}^{2/3}$. The number of nuclei in the target is related with the mass of the target as $N_{targ} \propto A_{targ}^{-1}$. These relations give us a production yield which is proportional to $\mathrm{A}_{targ}^{-1/3}$, with a fixed target. With this criteria, the lower-Z materials

will be the best targets. The election of the target has influence not only on the production yield, but also on the angular straggling and on the momentum spread. A special care and knowledge of the acceptance in the spectrometer is needed in this point.

An important characteristic of projectile fragmentation is the almost equal velocities of the produced fragments and the projectile. In the laboratory frame we observe all the fragments in a narrow-forward cone, making the detection and transportation of the fragments easier.

An useful and powerful tool for the fragment separation is based on the transport properties of charged particles under the effect of a magnetic field. It is based on the well known relation between the magnetic rigidity (Bρ, the product of the magnetic field applied in the magnet and the particle's curvature radius) and the momentum of the particle

$$B\rho = \frac{1}{e}\frac{Am_0}{Z}\beta\gamma c = \frac{1}{eZ}p \tag{1.1}$$

This simple equation gives a separation in A/Z for those particles with a known velocity. For further identification, an additional separation can be done with a degrader. This degrader is a piece of material placed in the flight path of the fragments. As far as the energy loss in a given material is proportional to Z^2, the fragments can be selected in charge measuring the energy loss in the degrader. Another possibility for lighter fragments will be the measurement of the *energy loss* in an ionization chamber.

There exist several attempts to modelize or to parametrize the momentum spread ($\sigma(P)$) of the fragments produced in this kind of reaction. The momentum distribution of the fragments in the rest frame fits well into a Gaussian distribution [11]. It is also proved that the parallel ($P_{\|}$) and perpendicular ($P_{\perp}$) momentum projections are identical in the rest frame. The momentum spread $\sigma(P_{\|})$ is almost independent on target mass and beam energy, but extremely dependent on the mass of the projectile (A_p) and the mass of the fragment (A_f). A theoretical approximation to this behavior was done by Goldhaber [11] and it is expressed as

$$\sigma(P_{\|}) = \sigma_0\sqrt{A_f(A_p - A_f)/(A_p - 1)} \tag{1.2}$$

where σ_0 $\approx$90 MeV/c. Another approach was done by Morrissey [10] in a semi empirical way. This approximation takes into account evaporation processes as far as many experimental results are included in the model. The Morrissey formula can be written as follows

$$\sigma(P_{\|}) = \frac{150}{\sqrt{3}}\sqrt{A_p - A_f} \tag{1.3}$$

1.2 Fields of Study

The possibility to perform experiments with radioactive nuclear beams gives a chance to get measurements in reactions with extreme conditions of isospin. The use of nuclei far from the line of stability helps to test models reaching their limits of application, or their whole validity. W

*Highly Excited States.*The production rate of high spin states is strongly dependent on the proton and neutron numbers of projectile and target nuclei. Using radioactive beams is possible to cover a large region in both quantities. These techniques not only provide the study of some of these states but high spin isomers with hundred ns of life-times could be produced as well. The production of long lived isomers allows to produce secondary beams to reach even higher spin states because large angular momentum can be induced into the fused system with less excitation energy. The limit of excitation is, in this way, increased.

Nuclear Astrophysics. Nucleosynthesis is supposed to be the source of all the elements that currently exist in the universe. The study of this process include the calculation of cross sections of low-energy reactions. Radioactive beams provide the chance to study many of these reactions, including radioactive capture reactions, such as (p, γ), or (n, γ). The cross sections of these reactions are known to be so small, so, in principle, high beam intensities are required. Recently the possibility of study these reactions in inverse Coulomb dissociation reactions helps to obtain some of these data.

Chapter 2

Experimental Setup

The experiment was performed in the FRagment Separator (*FRS*) [9], at Gesellschaft für SchwerIonenforschung (*GSI*), in Darmstadt, Germany. The FRS is a zero degree spectrometer, that can be also used as a separator to prepare secondary beams and perform with them precision experiments at its final focal plane, or drive them to other experimental areas, as it is showed in fig. 2.1. The primary beams are produced in the ion source, and accelerated in the UNILAC linear accelerator. These beams can be used in the low experimental area or can be guided to the synchrotron (*SIS*) to increase their energy. Then secondary beams can be produced by projectile fragmentation in a production target located at the entrance of the FRS. The FRS is used to separate and identify them. We give in this chapter a general description of the FRS spectrometer, pointing out how it was used to perform the present experiment. The detectors placed in the experimental area and their usage are also described.

2.1 The FRagment Separator FRS

The FRagment Separator is built in two symmetric stages in order to assure the achromatism of the whole system. Each stage includes two 30^o dipoles and a set of quadrupoles and sextupoles. The dipoles are used to bend the relativistic heavy ions inside the spectrometer, the magnetic rigidity available ranges from 5 Tm up to 18 Tm, with a maximum magnetic field of $B \simeq 1.6$ T. Doublets and triplets of quadrupoles are placed in front and behind of the dipoles. They help to illuminate the entrance to the dipoles, and to maximize the transmission through these bending magnets. The ion-optical system can be corrected for second-order aberrations placing sets of sextupoles at the exit and the entrance of the dipoles. The design

of the FRS allows to compensate the magnetic treatment of the beam done in the first stage with the second one, resulting an achromatic image of the beam in the final focal plane, at the exit of the spectrometer. The total length of the path inside the spectrometer is of about ∼70 m, where ∼6 m corresponds to each dipole. The figure 2.2 shows a simple layout of the FRS.

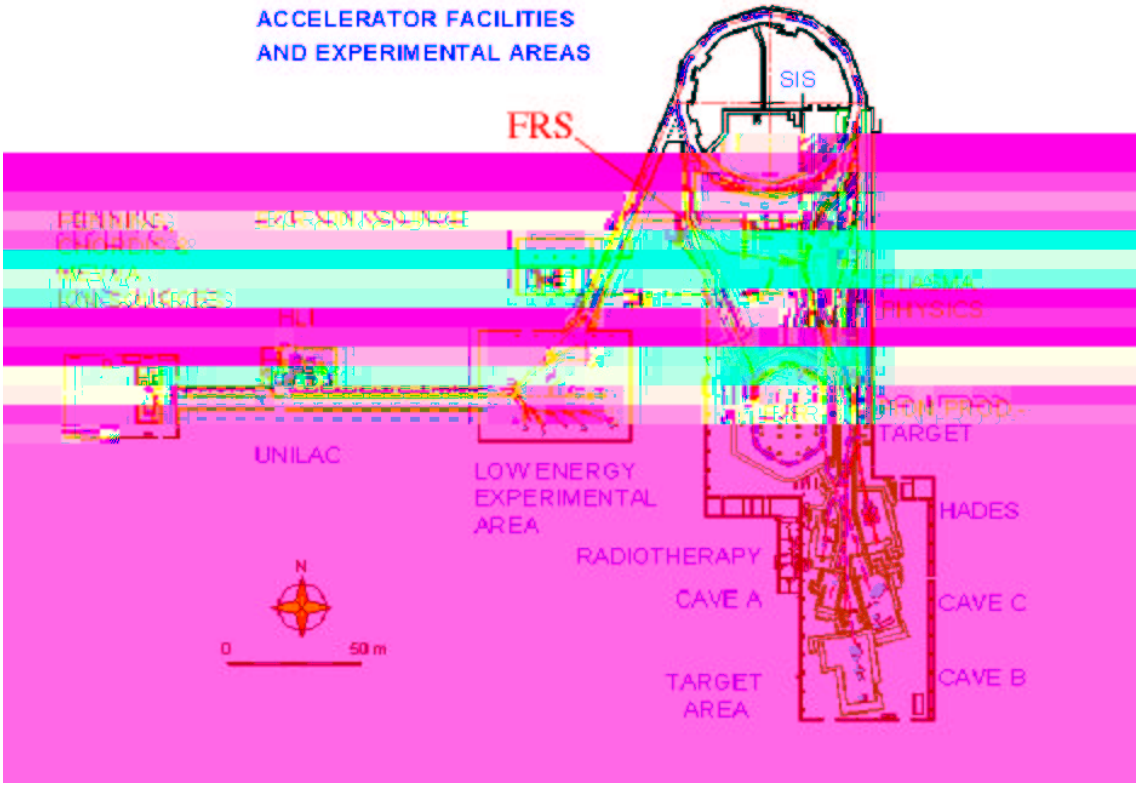

Figure 2.1: *The GSI facility is displayed in the figure. The beam starts to run in the ion source. Then is accelerated in the linear accelerator (UNILAC) up to the low energy experimental area. For further acceleration the beam can be driven to the synchrotron (SIS). The FRS experimental area can manage with the outgoing beam from the SIS. Then it is possible to prepare secondary beams, with species selected in the spectrometer, and to carry them from the FRS to other experimental areas, named CAVES in the figure.*

The design of the facility limits the acceptance of the spectrometer in magnetic rigidity and angle. The magnetic acceptance has a nominal value of $\Delta B\rho/B\rho$ ∼1.5 %, this value of the Bρ resolution was verified in several experiments. The angular acceptance is more related with the dimensions of the facility, and its nominal value is of $\Delta\theta \sim \pm 15$ mrad.

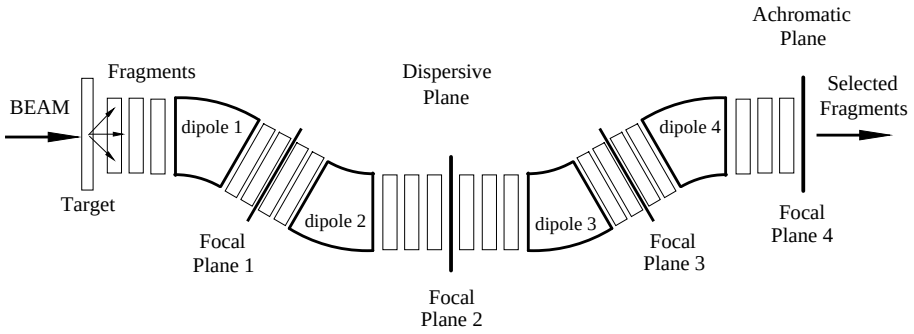

Figure 2.2: *We see in the figure the symmetric design of the FRS as well as the most important magnetic elements. The four dipoles are flanked with quadrupoles to illuminate the beam before bending and focus it at the exit of the dipoles to define the optimum ion-conditions at each image plane. Sextupoles used to correct aberrations are not included in the figure. The four focal planes are marked as well.*

The FRS has four focal planes, as we can see in fig. 2.2. The magnetic characteristics of the spectrometer are tuned in a way such that the position in these planes is related only to the momentum of the ingoing particles. The most important focal planes in the FRS are F2 and F4 (the middle one and the final one). In the achromatic mode, the beam particles reach the F4 plane without dispersion (the dispersion is defined as the variation of the position, x, with the momentum of a given particle compared with the momentum of a reference particle, δp, which runs in the central path, $\delta{=}\partial x/\partial\delta p$), independently on their energies or angles. This mode allows a refocalization of the beam at the exit of he FRS, and guarantees an optimal transmission of the secondary beams.

In the F2 plane the maximum dispersion is reached. The nominal value of the dispersion is δ=6.81 cm/%, but in this experiment the FRS is tuned to a dispersion of δ=4.34 cm/%. That is, if a particle runs with a Bρ 1 % greater than that of the central particle, at the F2 focal plane is separated by 4.34 cm from the central trajectory. Particles with the same momentum but different angles at the entrance of the FRS traverse the F2 plane in the same position.

The ion-optical characteristics of the spectrometer are define to get a good separation in momentum. The accuracy of this separation can be expressed with the *momentum resolving power*, defined at first order as $p/\Delta p{=}\delta/2\mathrm{Vx}_o$, where δ is the dispersion, V is the magnification, and x_o is the beam spot. The magnification is defined as the dependence of the position in the focal plane with the position in the entrance of the spectrometer, V=$\partial x_{F2}/\partial x_{ent}$, in this case V=0.79. With a beam spot of x_o=2.7 mm, and a dispersion of δ=4.38 cm/%, the momentum resolving power in F2 is $p/\Delta p$=1027. This value is slightly lower than the nominal value for

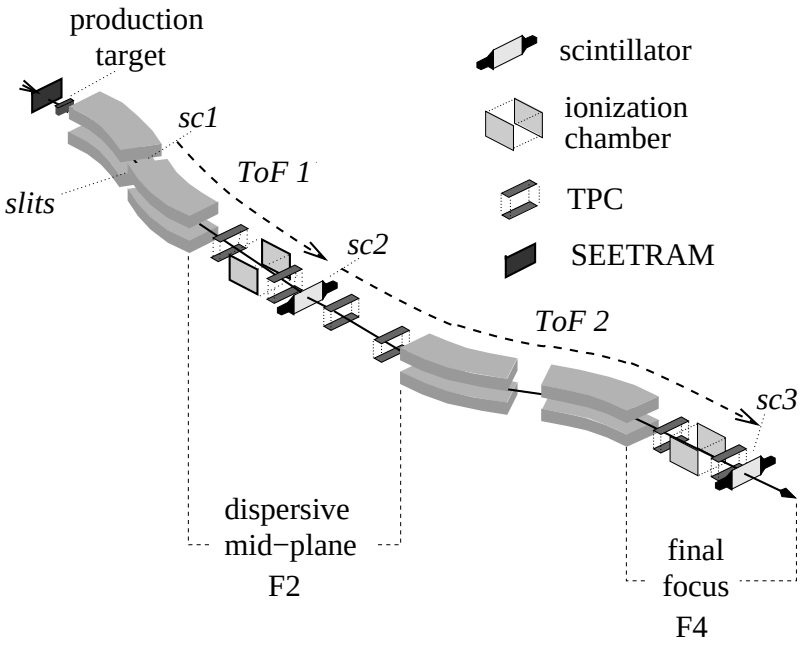

Figure 2.3: *Experimental setup used in the experiment. The primary-beam intensity is measured with the SEETRAM monitor placed in front of the target. Three plastic scintillators allow us to measure the time of flight in both sections of the spectrometer (ToF 1 and ToF 2). The nuclear charge is determined by means of their energy loss in two MUSIC detectors. With the information about position provided by TPC chambers we calculate mass over charge ratio for the different fragments.*

the FRS, $p/\Delta p$=1500, but enough to achieve a good separation, as we see in this work.

2.2 Detectors

We present in fig. 2.3 a schematic view of the FRS with the detectors used in this experiment. A description of each one, together with the physical quantity they measure and the data reduced from these measurements, is given.

The number of incident particles is measured through an incident beam monitor, that gives a signal proportional to the number of particles in the primary beam. The complete identification of the fragments is achieved via an A/Z and Z determination. The position distributions at the focal planes is related with the Bρ of the particles, and their Bρ is proportional to the mass over charge ratio. Position detectors (*TPCs*) are used to determine the A/Z ratio of the produced fragments.

Ionization chambers (*MUSICs*) are used to get information about the charges of the fragments through their energy deposition. The Bethe-Bohr model provides the relation between the *energy deposition* and the charge and velocity of the ionizing particle. The velocities of the fragments are calculated from their Time of Flight (*ToF*) through the spectrometer recorded by plastic scintillators (*SCIs*) and allows mass determination.

2.2.1 Beam Monitor

To monitoring the beam, the SEcondary Electron TRAnsmission Monitor (*SEETRAM*) [15] is used. This extremely non interactive detector avoid the problems related with the measure of the beam current through beam stop when relativistic energies are applied. The production of secondary products, that can contaminate the beam, from the stopping process does not longer appear.

The SEETRAM consists in three *Al* foils, in a vacuum environment, placed in front of the target. The outer layers are connected to a 80 V positive voltage, while the inner layer is set to the ground reference. The three layers are bended to reduce the sensitivity to mechanical vibrations of the beam line. A simple drawing of this detector is shown in fig. 2.4.

The beam monitoring is based on the emission of secondary electrons produced by relativistic ions traversing the foils. The produced secondary electrons are driven to the outer foils by the action of the positive voltage. The resulting positive current in the inner layer is measured by a current digitizer. A current integrator transforms the charge collected into a signal with a proportional amplitude.

The signal produced is then proportional to the number of particles going through the monitor.

2.2.2 Time Projection Chambers

Position sensitive detectors are used to determine the momentum distribution by using the existing ratio between the horizontal position in F2 focal plane with the momentum of the particle (through the dispersion, δ). In the present experimental setup the detectors used to measure the positions of the different fragments at F2 plane are Time Projection Chambers, (*TPC*) [16]. These detectors allow to determine x and y position with a resolution better than 0.5 mm.

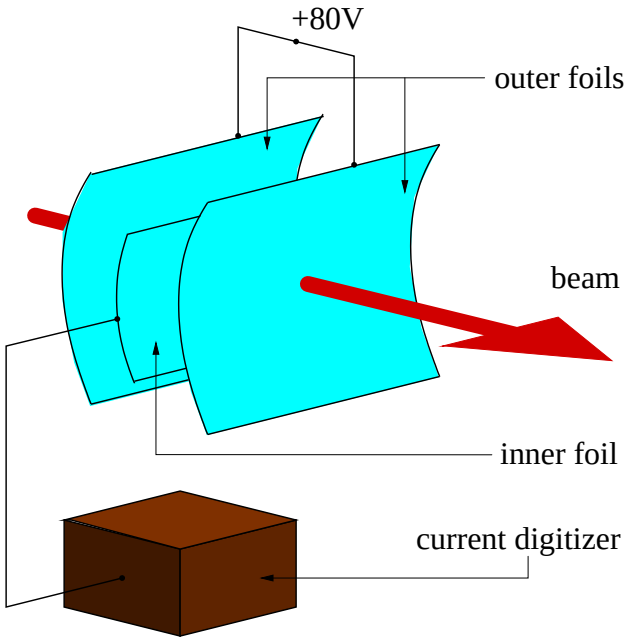

Figure 2.4: *A simple picture of the SEETRAM where the curved layers and the current digitizer are shown.*

The Time Projection Chambers consist on a drift space, filled with P10 gas (90% Ar + 10% CH_4), in an uniform electric field, and four proportional counters that work as anodes, with a frisch grid over them. A schematic view is depicted in fig. 2.5. When an ionizing particle traverses the drift space the free cloud of electrons produced, runs as a cascade from the track of the particle to the frisch grid, where the electrons are accelerated to the proportional chambers that surround each anode wire.

The drift time of the electrons is used to deduce the vertical y position. When the electrons reach the anodes an induced pulse is recorded by a delay line placed below the anode wires. The pulse is transmitted to the left and right sides, the horizontal position can be calculated through the time difference between the arrival of both signals. The measurement of the position with two TPC allows to determine the angle of each ion, in the F2 focal plane, as well. In fig. 2.6 a representation of the horizontal and vertical position and angle distributions at F2, measured by the TPCs, is presented.

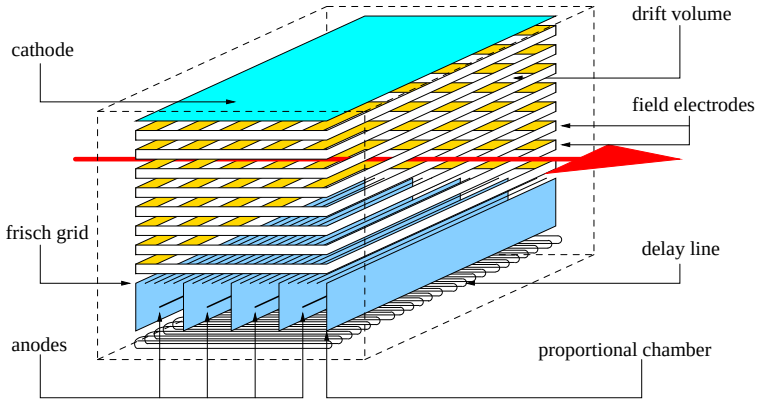

Figure 2.5: *Schematic layout of the Time Projection Chamber (TPC). The electrons produced by an ionizing particle are guided by the electric field and accelerated in the frisch grid, reaching a higher ionization near the anodes. The charge collected in the anodes induce a positive charge current in the delay line. The arrival times at both ends of the delay line are recorded in order to determine the x position, while the drift time of the electrons to the anode wires is used to deduce the y position.*

2.2.3 MUltiple Sampling Ionization Chamber

We use a MUltiple Sampling Ionization Chamber (*MUSIC*) [17][18] to determine the atomic number of the fragments produced, by measuring their energy deposition. We place two different MUSIC detectors, one located at F2 and the other at F4 to identify in atomic number in both sectors of the FRS.

The MUSIC is designed as a parallel-plate ionization chamber, with a drift volume filled with P10 gas (90% Ar + 10% CH_4), in an uniform electric field, as the TPC. When an ionizing particle pass through the drift volume a cloud of ions and free electrons is created. The cloud of electrons is accelerated in a frisch grid placed in front of the field anodes, and collected in these anodes, then charge sensitive preamplifiers give a signal in which its amplitude is proportional to the number of electrons collected. In fig. 2.7 the MUSIC is schematically described.

The Bethe formula, in first order approximation gives a relation between the atomic number of the particle and its velocity with the *specific energy loss*

$$-\frac{dE}{ds} = \frac{4\pi Z_p^2}{m_e u v^2}\left(\frac{e^2}{4\pi\varepsilon_0}\right)^2 Z_t N_t L \tag{2.1}$$

where the stopping number L, is defined as

$$L = ln\frac{2m_e v^2}{I} - ln(1-\beta^2) - \beta^2 \tag{2.2}$$

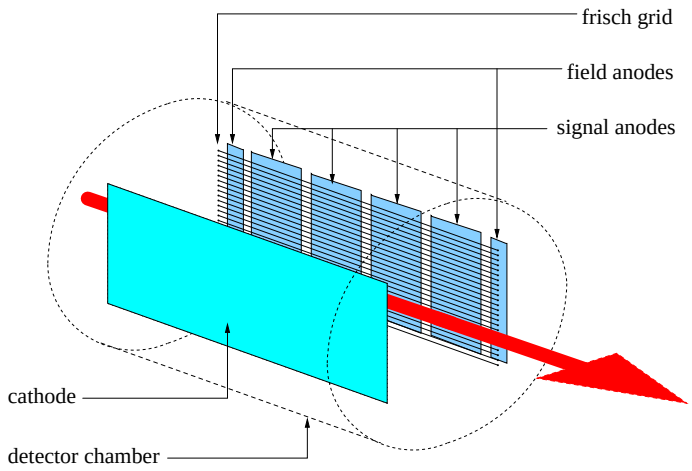

Figure 2.7: *The MUltiple Sampling Ionization Chamber (MUSIC) is depicted in this figure. The electron shower produced by an ionizing particle through the drift space is collected in the signal anodes after the electrons acceleration in the frisch grid. This signal is proportional to the energy deposited in the active area of the detector. The atomic number of the particle is related to the energy loss and its velocity through the Bethe formula.*

with photo multipliers in both left and right sides of the SCI, the difference between the recollection times can be used to deduced the x position. In this work, they are only used as timing detectors.

The signal coming from the first SCI, placed at the first focal plane (F1), is the stop of the Time of Flight (*TOF*) from F1 to F2, where a second SCI is used as start of this ToF, and as a stop of a second ToF, between F2 and F4 plane, where a third SCI is placed. The calculation of the velocity of the fragments produced is done in both parts of the FRS (see fig. 2.3).

The SCIs provide the timing [19] to the TPCs, as well. The measurement of the electrons drift time has its start in the SCI signal.

In fig. 2.8 we present the identification plots obtained for a particular setting of this experiment in both sectors of the FRS. The main difference between these two spectra is a better A/Z resolution, obtained with the longer ToF in the second half of the spectrometer.

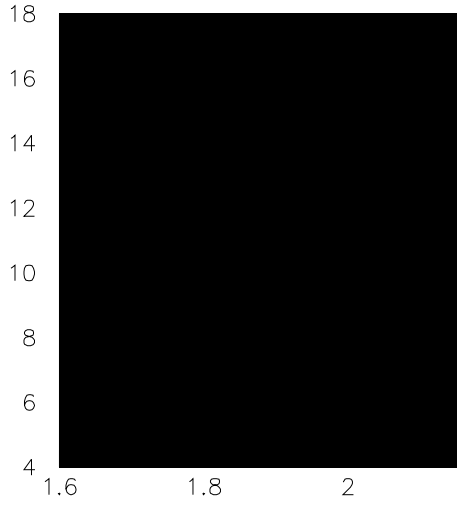
18
16
14
12
10
8
6
4
1.6
1.8
2

Chapter 3

Data Analysis

In this chapter we present the experimental data analysis. The aim of this work is the determination of the production cross section of the identified isotopes in the fragmentation of a ^{36}Ar primary beam on a ^{9}Be 1625 mg/cm^2, at 1050 A·MeV. Production cross sections are given by the ratio between fragments produced in the reaction and incident particles impinging on the target, normalized by the number of atoms in the production target. The number of incident nucleus is measured by using an incident beam monitor, as we show in section 3.1. In section 3.2 we explain the identification method and determination of the number of produced fragments. In section 3.3 the normalization to the number of atoms in the target is presented. However, it is necessary to apply certain corrections before giving the final production cross section, σ_{prod}. These corrections are explained in section 3.4. Finally, in section 3.5, we discuss the uncertainties of the measurement.

3.1 The Incident Beam Monitor

To measure the number of incident particles an extremely non interactive detector is used all over the experiment. In our particular case this is a SEcondary Electron TRAnsmission Monitor (*SEETRAM*) [15]. This detector gives a signal, through the collection of the secondary electrons produced, proportional to the number of ions passing through it, as it is shown in chapter 2. We calibrate this signal to determine the number of incident projectiles.

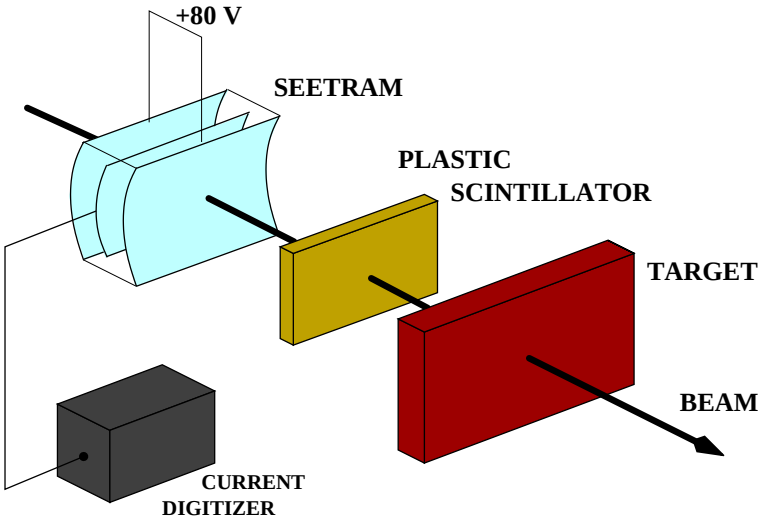

Figure 3.1: *The plastic scintillator (SCI) is placed between the SEETRAM and the target during the calibration. The current signal of the SEETRAM is digitized in order to have equivalent counts, these counts are recorded with the particle counting coming from the SCI. In the analysis these two signals are compared for different values of the beam intensity for calibration purposes.*

3.1.1 Calibration of the Incident Beam Monitor

The first step is to calibrate the monitor. Since the secondary-electron current of the SEETRAM is assumed to be proportional to the primary-beam current we can compare this signal with the number of particles counted with an additional detector system, in this case, a plastic scintillator (*SCI*). We place the SCI just after the SEETRAM, as we see in fig. 3.1. Those two signals are recorded for different values of the beam intensity, covering the maximal kinetic range. Due to the pulsed nature of GSI beams, all signals recorded will have a peak structure appearance, as it is shown in fig. 3.2. In the analysis of the data the number of particles measured by the SCI is integrated over one spill as well as the number of the SEETRAM inside the same spill. As it can be observed in fig. 3.2, for the SEETRAM a quasi-constant level appears in between the pulses. This level corresponds to background noise due to a dark current in the digitizer. The SEETRAM gives a signal related to the current of the secondary electrons produced by the passage of a charged particle, but a small current of electrons is produced inside the detector, even without the hit of any particle [20]. In fact, an offset in the acquisition is tuned to display this dark current, in order to have the possibility of a further substraction. We evaluate these background counts to substract them from the integral of the pulses as we explain in the next section.

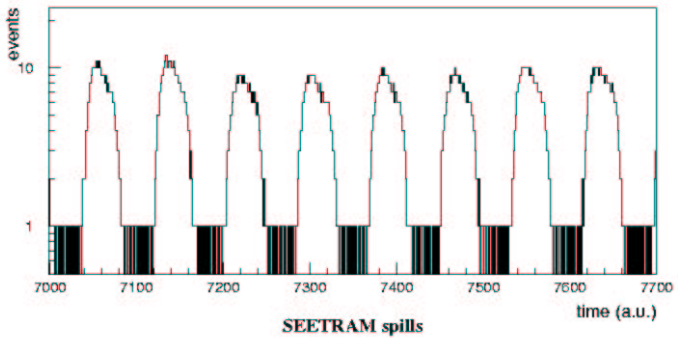

Figure 3.2: *SEETRAM equivalent counts as a function of time, for a certain time interval during the calibration. The x-axis channels correspond to time in arbitrary units. The spills have a length of* $\sim$ *8 s with a period of* $\sim$ *16 s. The constant level of the dark current is also clear between the pulses.*

In fig. 3.3 we plot the value of this spill integral in both detectors for many individual spills, that is, the number of projectiles measured with the plastic scintillator versus the equivalent counts of the SEETRAM, in a wide range of intensity. We observe, for lower intensities, a linear relation between the number of particles given by the plastic and the equivalent counts in the SEETRAM, this relation disappears as the intensity increases. This behavior is due to saturation phenomena in the SCI. While the SEETRAM has a good response to high intensity the scintillator begins to saturate, and the signal from the SEETRAM is no longer proportional to the scintillator lecture. In principle, plastic detectors work well up to counting rates around 10^5 particles per second where the saturation effects start to be remarkable.

For primary beam intensities higher than 10^{+7} pps we need to extend the SEETRAM calibration with other detectors. In the FRS an Ionization Chamber for high counting rates, from 10^{-12} A up to 10^{-7} A, is used [21]. The procedure is the following: in a first step the IC current is calibrated by particle counting. Secondly, the SEETRAM current is calibrated with respect to the IC current. The two calibrations, with the SCI and with the IC, overlap and cover the whole intensity range needed. Due to the lack of time we decided to skip this careful calibration in this experiment. We take as SEETRAM calibration the results of the linear fit performed with the data shown in fig. 3.3.

Under these conditions it is very important to find the limits, where the saturation of our SCI starts, that will provide the right calibration. Our method to decide it is to perform a linear regression over different intensity ranges and plot

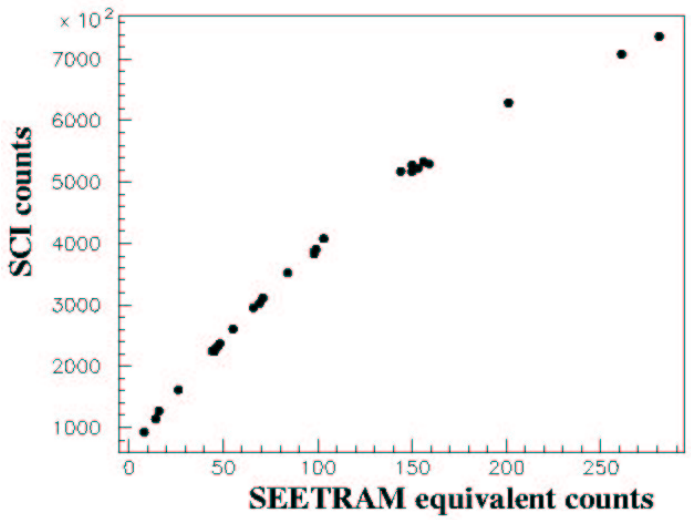

Figure 3.3: *We represent in this picture the number of counts in each spill for different values of the intensity in the SCI plotted versus the equivalent counting rate in the SEETRAM. The linear relation for lower intensities and the effect of saturation at higher intensities appears clearly.*

the slope of the different linear fits versus the number of points used for them. In fig. 3.4 we see such a plot, where the number of points are always taken from the lower intensity available. We can observe a plateau between the equivalent SEETRAM counts 6 to 10, corresponding to the region where the linear behavior of our scintillator is ensured. We choose as final calibration the mean value of the slope in this region, weighted by their corresponding error. The result is a slope of 3571 ± 5 ions/SEETRAM. This result is in good agreement with other calibrations done recently for the same SEETRAM, as we show in fig. 3.12.

3.1.2 Background substraction

In the previous section we talk about the substraction of the background counting produced in the SEETRAM due to the production of electrons even when there is no particle passing through the monitor. The method used to set the value of the background noise is a simple projection of the histogram containing the pulses of counts versus time in the counts axis. That is, we project the histograms such as that of fig. 3.2 for each setting in the number of counts axis. This projection has a

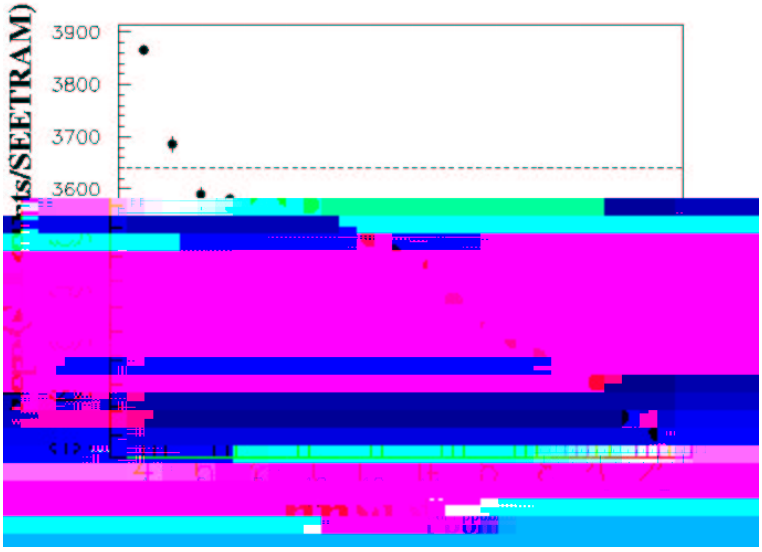

Figure 3.4: *We show in this picture the number of points used for different SEETRAM calibrations versus the slope of the linear fit performed. In order to choose the best calibration we look for a region where the relation between the SCI counts and the SEETRAM signal is linear. The plateau observed between the calibrations performed with 6 to 10 corresponds to our choice of "best calibration". The horizontal lines mark the mean value with its error.*

peak centered in the noise average value. Fitting this peak to a Gaussian function we take the mean value of the peak as the level of noise to substract and the standard deviation σ^2 as its uncertainty. This procedure is showed in fig. 3.9.

The uncertainty corresponds to a typical value of 5 % of the background noise level, but this uncertainty is up to four orders of magnitude lower than to the number of incident particles. This percentage in the uncertainty of the background substraction does not contribute to the total uncertainty of the calculation due to its small value.

3.2 Fragments Identification

The experimental set up allows the identification of the fragments, in atomic number and mass, in both stages: from F1 to F2, and F2 to F4. In the present work we use only the measurements done at the first stage. This decision has some advantages:

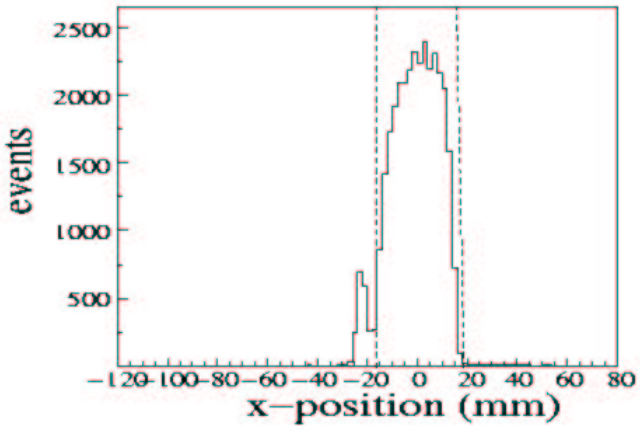

Figure 3.5: *Position distribution of a given fragment at the F2 focal plane obtained from the TPC chambers. The distribution is truncated by the action of the slits placed at S1 (dashed line). We can only see a small portion of the entire position distribution.*

transmission losses are more important in the second stage, bigger corrections are needed to compensate this effect, and, consequently, the uncertainties increase. The election of the first stage provides a better resolution in position, as far as the achromatism in F4 is not perfect, that is, the dispersion from F2 to F4 (δ_{F2-F4}=4.98 cm/%) does not compensate totally that from the target to F2 (δ_{F0-F2}=4.34 cm/%), and the treatment of data turns more complicated and with bigger asociated errors. On the other hand, disadvantages also appear: the ToF distance of the first stage is shorter than the second one, that means less precision in A/Z determination. Nevertheless, we achieve a good separation in both, mass and mass over charge ratio, as we see in fig. 3.10.

Once the identification of all the fragments is done (see section 2.2), we generate two-dimensional histograms of the Z of the fragments in F2 versus their mass over charge ratio for each setting, one of these is presented in fig. 3.11. We select the different identified fragments, making cuts in mass and charge distribution histograms, in order to have the number of each produced isotope, N_p.

The settings cover different magnetic fields up to regions where we identify fragments placed at the proton drip-line in the nuclear chart. This region is easily recognized by the "holes" in the identification matrices corresponding to unbound nuclei (fig. 3.11).

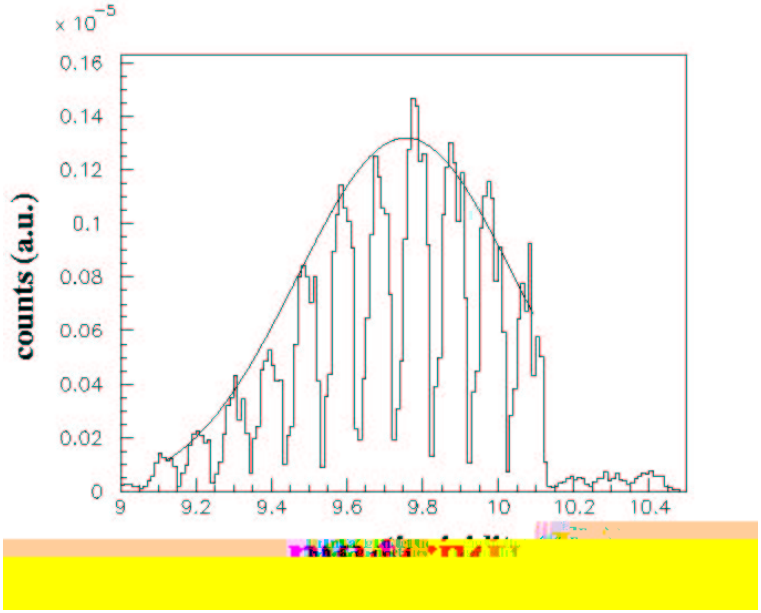

Figure 3.6: *Reconstruction of the Bρ distribution of ^{14}O. The different settings do not overlap in the plot and the "holes" appear. We present the fit to a Gaussian shape, used in this case to extract the corresponding cross section value.*

3.2.1 Beam Reconstruction and Normalization

As it has been showed in fig. 2.3, a small scintillator at focal plane S1 is placed in the experimental setup. The position slits S1 placed in front of the S1 scintillator are closed up to +9,-8 mm, in order to cut the beam that is not passing through the SCI. The effect of these closed slits is translated in important transmission losses. Moreover, the momentum distribution of the produced fragments are extremely cut in each individual setting. This effect is represented in fig. 3.5. We can go through this problem reconstructing the beam profile over the different settings to recover the complete Bρ and momentum distributions. Both quantities are related in the case of an uniform magnetic field by the formula

$$B\rho = \frac{1}{e}\frac{Am_0}{Z}\beta\gamma c = \frac{1}{eZ}p \tag{3.1}$$

The Bρ calculation is performed from a position measurement using the equation

$$B\rho = B\rho_0\left(1+\frac{x}{\delta}\right) \tag{3.2}$$

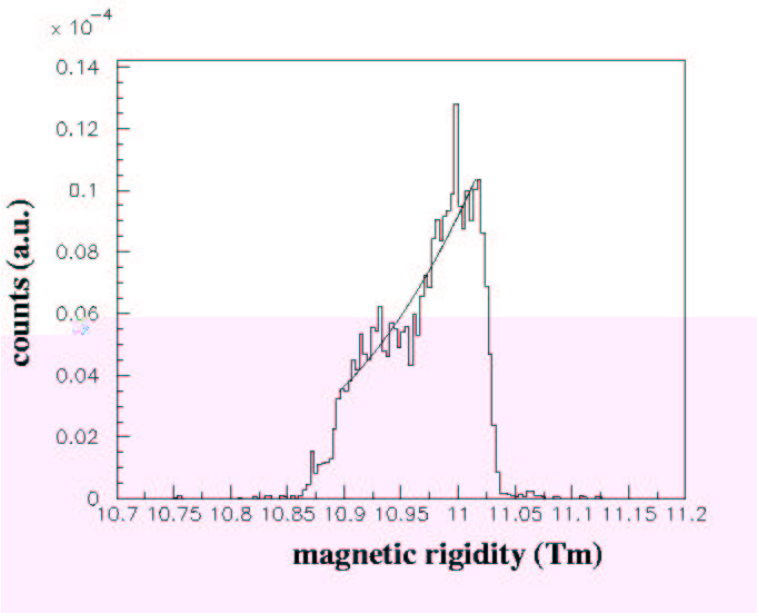

Figure 3.7: *Another example of a Bρ distribution is shown in this picture. The distribution of some isotopes (^{18}F in this case) is not always complete, and the goodness of the fit is not guaranteed.*

Where Bρ_0 is the magnetic rigidity of a reference particle whichs follows the central trajectory in the spectrometer, x is the position measured in the focal plane F2, and δ is the so-called dispersion. This quantity depends on the optical characteristics of the spectrometer, and, in our case, it has a value $\delta_{(target-S2)}$= -4.337721 cm/% . Each Bρ distribution section was normalized to the number of incident particles, given by the SEETRAM, since this number is different for each setting. When we plot together the magnetic rigidity distributions of each isotope we can see the complete momentum distribution, as it is showed in fig. 3.6. The reconstruction of the complete Bρ distribution of each fragment is done in this way.

3.2.2 Evaluation of cross sections. Numerical Integral

In order to get the total rate between produced fragments and incident projectiles of one single isotope we cannot simply count the number of events that rise from the plot (fig. 3.6), but we have to recover the "holes" that appear in the reconstruction. These holes appear due to the fact that the scanning is done by steps without overlap, as we explain before.

These Bρ distributions follow a Gaussian shape [11]. We can fit them to this function to recover the complete distributions. To perform this fit we take only the points where we are sure that they are not in the region corresponding to positions cut by the slits. Once the fit is done we can integrate these Gaussian fits to get the total rate. These integrals have to be numerical integrals, not analytic, since the distributions are processed as histograms. We have to take care about the binning of the histograms and doing the integral as a sum of finite steps. These steps have the size of the corresponding binning for each histogram. The numerical integral is given by the expression

$$I = C \cdot \sum_{i=a}^{b} exp\left[-\left(\mu - x_i\right)^2 / 2\sigma^2\right] \tag{3.3}$$

Where I is the evaluated integral, C is the constant corresponding to the maximum of the Gaussian distribution, μ is the mean value of the distribution, and σ^2 is the variance. The steps of the sum are defined by $x_i = a + i \cdot \Delta x$, where Δx is the bin of the histogram, and a and b are the limits of the sum , they are taken as more than ten times σ, far enough to get a good result.

In some cases the reconstructions have only few settings, this implies that the fit is not necessary good (fig. 3.7). In these cases the fit is forced fixing two of its parameters. There are three parameters to fit: C, μ and $\sigma_{B\rho}$. As we are discussing about Bρ distributions, μ will be the mean value of the magnetic rigidity, $\bar{B\rho}$. This is related with the velocity through

$$v = \frac{c}{\sqrt{1 + \left(\frac{Am_0c}{B\rho Z}\right)^2}} \tag{3.4}$$

That is, the velocity of each isotope is a function of $B\rho Z/A=$

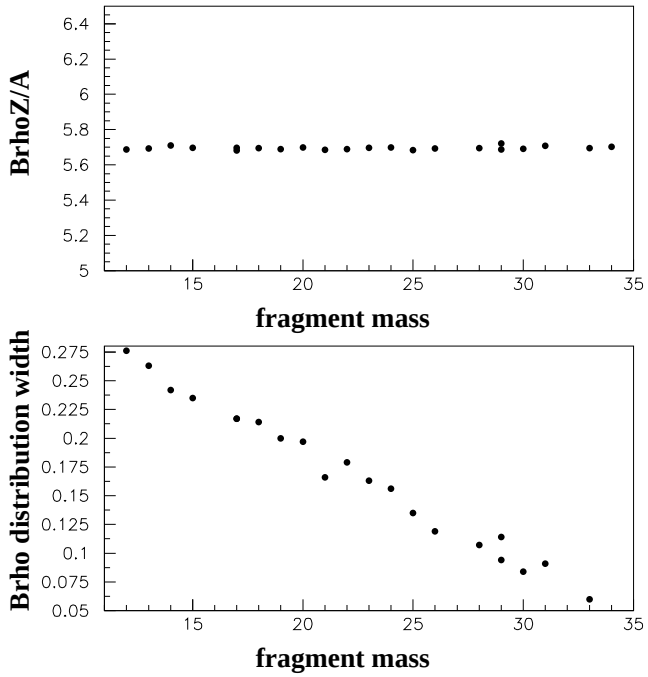

Figure 3.8: *The BρZ/A value for each produced isotope mass is plotted in the upper figure. From this plot we can interpolate the mean value of the Bρ for the case of distributions with a low number of settings. We can see how the value of BρZ/A is almost constant. The lower figure shows the width of the Bρ distributions versus the mass of the produced fragments. A predicted value for $\sigma_{B\rho}$is deduced for those truncated distributions.*

3.3 Target Factor

The concept of production cross section is related with the probability of a given reaction channel after the collision between one projectile particle and one target particle. In the experiment we use a beam of projectiles and a great number of atoms in the target. The normalization to the number of projectiles is done with the SEETRAM when we reconstruct the Bρ distributions. The number of atoms in the target is evaluated through the target factor, T_f

$$T_f = \frac{T_{thickness} \cdot N_A}{m_{target}} \tag{3.6}$$

Where $T_{thickness}$ is the thickness of the target, N_A is the Avogadro number, and m_{target} is the nuclear mass of the target.

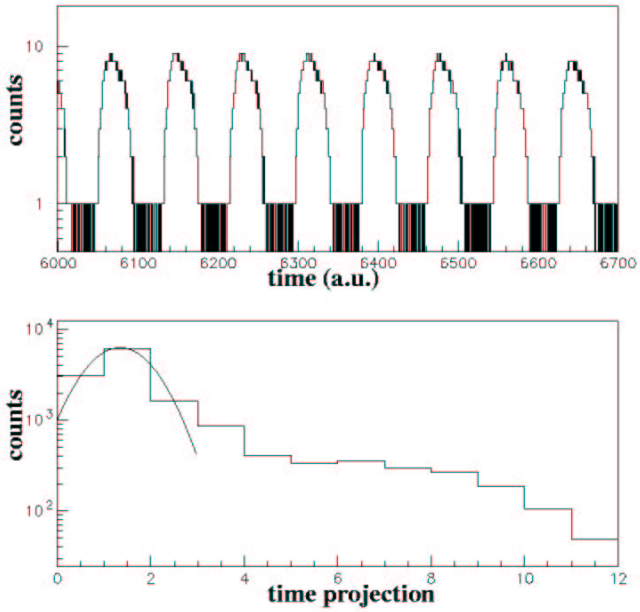

Figure 3.9: *In the upper plot we see a histogram showing the pulsed structure of GSI beams from the SEETRAM counters, similar to the one showed in fig.*3.2. *The lower figure is the projection of that histogram in y-axis. The peak corresponding to the noise level appears clearly, and over it the Gaussian fit is drawn.*

This factor, T_f, gives the total ratio between reaction products and incident projectiles in mb. In this experiment the target is a foil of ^{9}Be with $mass_{Be}$=9.012182 u and a thickness $T_{thickness}$=1.625 g/cm^2. The factor is finally T_f=0.1086 mb^{-1}.

3.4 Corrections

In order to calculate the ratio between the number of produced and incident particles independently from the experimental setup, we have to take into account all the particles which are lost or not detected, due to the experimental set up. For this reason some corrections need to be applied.

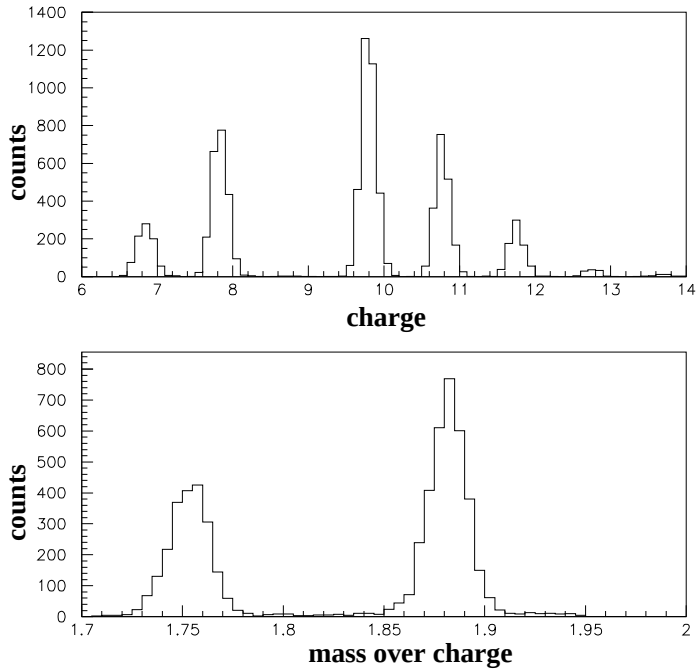

Figure 3.10: *The upper figure shows the charge resolution for a given setting, in the lower figure appears the mass over charge resolution, for a fixed atomic number, in the same setting. A good separation is achieve in both quantities.*

3.4.1 Dead Time

The data acquisition requires some time to process each event. During this time, the acquisition cannot process new events. This is the so-called dead time. The dead time was determined as a ratio via two scalers. One scaler recorded all the triggers independently of the data acquisition, whereas the second one detected only those that were registered by the data acquisition. The ratio between the processed triggers to the total gives the correction factor for the dead time, D_t.

In table 3.1 we show the value of the dead time for every setting in this experiment. The dead time runs from $\sim$75%, from the most stable settings, up to $\sim$55% in the settings where the proton drip line is reached, where the production cross sections, and so the number of events, decrease.

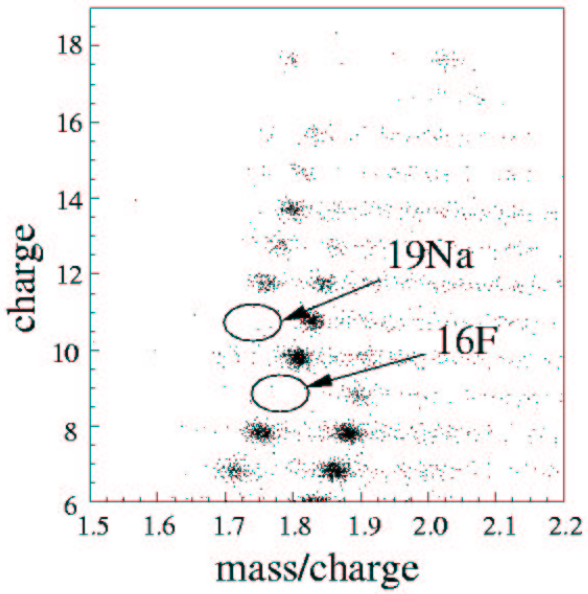

Figure 3.11: *The figure shows an A-A/Z matrix for a certain setting. In this case the proton drip-line is reached. The "holes" corresponding to the unbound nuclei* ^{16}F *and* ^{19}Na *appear clearly.*

3.4.2 Transmission

In order to calculate the production cross section, σ_p, we measure the number of fragments in F2 plane. This quantity is not equal to the number of produced fragments in the target. Some of the isotopes produced in the fragmentation are not transmitted up to F2, due to the limited acceptance of the spectrometer in momentum and angle. In order to correct these losses we need to estimate the transmission of the FRS in this experiment. We use a method recently developed to calculate the angular transmission [22], since the longitudinal momentum acceptance is overcome by combining different magnetic settings.

In the method we used, the angular acceptance is formulated in terms of a few optical characteristic parameters, this map of the effective angular acceptance is valid for any reaction studied in the spectrometer. The angular distribution depends on the kinematics of the reaction that take place.

The kinematics of the reaction can be calculated through the measurement of the longitudinal and transversal components of the momentum in laboratory frame. We can only measure the longitudinal momentum in the spectrometer, but, since

$B\rho\ (Tm)$	$DeadTime\ (\%)$	$B\rho\ (Tm)$	$DeadTime\ (\%)$
10.92	55	9.87	65
10.81	66	9.78	69
10.70	66	9.68	60
10.60	66	9.58	63
10.49	64	9.49	66
10.38	63	9.39	57
10.28	62	9.30	63
10.18	51	9.20	68
10.08	55	9.11	75
9.97	60		

Table 3.1: *The dead time is displayed in this table as the percentage of lost events. The different settings are listed by their Bρ value.*

the longitudinal and transversal components of the momentum in the rest frame are suppose to be the same, the transversal momentum in laboratory frame can be deduced.

The reconstructed Bρ distributions are translated to momentum in rest frame. The rest frame transformation is done implementing the incident beam in the middle of the target, as a mean value of the place where the reactions occur. Then the transversal projection of the momentum in the rest frame is deduced and transformed into the laboratory frame. The angular distribution is then calculated and compared with the angular acceptance of the spectrometer, in order to determine the angular transmission losses.

Table 3.2 resumes the value for the angular transmission for each isotope in percentage units. The biggest corrections are applied to the lightest isotopes.

3.5 Uncertainties

In this work the main uncertainty sources come from the beam reconstruction and the calculation of the total area in the Bρ distribution. These uncertainties are related with the three parameters of the fits: the constant C (with its corresponding uncertainty $\epsilon(C)$), the variance σ ($\epsilon(\sigma)$), and the mean value μ ($\epsilon(\mu)$). The calibration of the SEETRAM is another source of uncertainty due to the error gave in its calibration ($\epsilon(Seet)$). The correction related with the transmission of the spectrometer ($\epsilon(Tr)$) contributes to increase the uncertainty of the final result, as well as the

$Isotope$	$Trans(\%)$	$Isotope$	$Trans(\%)$	$Isotope$	$Trans(\%)$
^{12}N	33	^{20}Ne	66	^{27}P	97
^{13}N	33	^{21}Mg	73	^{27}Si	92
^{13}O	41	^{21}Na	77	^{28}P	97
^{14}O	42	^{22}Al	76	^{29}P	99
^{15}O	49	^{22}Mg	72	^{29}S	98
^{16}O	51	^{22}Na	67	^{30}S	99
^{17}F	51	^{23}Al	84	^{31}Cl	100
^{17}Ne	52	^{23}Mg	75	^{31}S	100
^{18}F	62	^{24}Al	81	^{32}Cl	100
^{18}Ne	56	^{24}Si	85	^{33}Ar	100
^{19}Ne	66	^{25}Al	85	^{33}Cl	100
^{20}Mg	75	^{25}Si	88	^{34}Ar	100
^{20}Na	61	^{26}Si	93		

Table 3.2: *This table shows the different transmission for each fragment in percentage units.*

common statistical uncertainty ($\epsilon(Stat)$).

The relative uncertainty ϵ of the cross section is calculated as a quadratic sum of the relative uncertainties of the different components:

$$\epsilon^2_{total}(\sigma_p) = \epsilon^2(Tra) + \epsilon^2(Stat) + \epsilon^2(Seet) + \epsilon^2(C) + \epsilon^2(\sigma) + \epsilon^2(\mu) \tag{3.7}$$

We describe these uncertainties in the following subsections. In table 3.3 the components and the final value of the uncertainties expressed in % for each isotope are summarized.

3.5.1 Statistical uncertainty

As a random process, we treat the collection of data with the Poisson probability function. The variance σ^2 is then equal to the mean value, that is, the number of events, N_{ev}. The uncertainty assigned to each calculation is the square of the number of events collected $\sigma = \sqrt{(N_{ev})}$, and the statistical uncertainty $\epsilon(Stat) = N_{ev}/\sqrt{(N_{ev})}$.

$Isotope$	$\epsilon(Tra)$	$\epsilon(Stat)$	$\epsilon(Seet)$	$\epsilon(C)$	$\epsilon(\mu)$	$\epsilon(\sigma)$	$\epsilon_{total}(\sigma_p)$ %
^{12}N	1	0.4	2	2	0.1	1	3
^{13}N	4	0.3	2	*	*	*	32
^{13}O	1	0.3	2	2	0.1	3	4
^{14}O	1	0.3	2	2	0.1	1	3
^{15}O	1	0.1	2	2	0.1	1	3
^{16}O	4	0.1	2	12	0.2	11	17
^{17}F	1	0.1	2	2	0.1	1	3
^{17}Ne	1	0.1	2	2	0.1	1	3
^{18}F	4	0.1	2	13	0.2	12	18
^{18}Ne	1	0.1	2	2	0.1	1	3
^{19}Ne	1	0.1	2	2	0.1	1	3
^{20}Mg	3	0.1	2	3	0.3	15	17
^{20}Na	1	0.1	2	2	0.1	1	3
^{20}Ne	1	0.1	2	*	*	*	22
^{21}Mg	3	0.1	2	16	0.5	13	21
^{21}Na	3	0.1	2	3	0.1	14	14
^{22}Al	3	0.1	2	2	0.1	13	13
^{22}Mg	1	0.1	2	3	0.1	1	4
^{22}Na	1	0.1	2	*	*	*	31
^{23}Al	2	0.1	2	2	0.1	14	14
^{23}Mg	1	0.1	2	1	0.1	2	3
^{24}Al	1	0.1	2	3	0.1	1	4
^{24}Si	5	0.1	2	49	0.2	32	59
^{25}Al	3	0.1	2	2	0.1	14	15
^{25}Si	1	0.1	2	2	0.1	1	3
^{26}Si	1	0.1	2	2	0.1	1	3
^{27}P	1	0.1	2	2	0.1	19	20
^{27}Si	1	0.1	2	3	0.1	16	17
^{28}P	1	0.1	2	3	0.1	1	4
^{29}P	1	0.1	2	6	0.1	1	6
^{29}S	1	0.1	2	2	0.1	1	3
^{30}S	1	0.1	2	3	0.1	1	4
^{31}Cl	1	0.1	2	3	0.1	31	30
^{31}S	1	0.1	2	3	0.1	9	9
^{32}Cl	1	0.1	2	3	0.1	29	30
^{33}Ar	1	0.1	2	2	0.1	0.1	3
^{33}Cl	1	0.1	2	3	0.2	28	28
^{34}Ar	1	0.1	2	2	0.1	1	3

Table 3.3: *The uncertainties are summarized in this table. The different components and the total error are displayed in percentage of the final σ_p. The * mark those estimated errors (see text for details)*

3.5.2 Seetram Calibration

In section 2.1 we explain the SEETRAM calibration. This calibration has an uncertainty that affects the determination of the production cross section. The slope of the fit is 3571±5 ions/SEETRAM, then the uncertainty is 5/3571 ≈0.2 % in the ratio between the signal in the SEETRAM and the counts from the SCI. This method of calibration has other sources of systematic errors: the irregular spill shapes that lead to fluctuating recombination losses and recombination effects in the ionisation current. The substracting of the offset (dark current of the SEETRAM counter) increases this uncertainty. The final error induced by these effects is estimated to be smaller than 2 % [20]. For this experiment we take $\epsilon(Seet)$=2 %.

3.5.3 Numeric Integral

The uncertainty in the numeric integral arises mainly from the uncertainty in the three parameters of the fit: the constant C, the variance σ^2, and the mean μ, which, in this case, corresponds to the mean value of the magnetic rigidity $\bar{B\rho}$. In the cases where the fit is forced choosing the mean $\bar{B\rho}$, and the width $\sigma_{B\rho}$, the error is determined by the error associated to each parameter and the range of the mean $\bar{B\rho}$, and the width $\sigma_{B\rho}$, estimated values.

3.5.4 Transmission Through the FRS

The calculation of the angular acceptance and transmission needs an exact geometrical description of the spectrometer. The dimensions used in the method described in section 3.4.2 are taken from the plans of the FRS, and there were found discrepancies with the real sizes in the FRS of about 2 mm, associated to deformations in the inner tubes. These discrepancies lead in the calculations to an uncertainty of about ∼0.5 %.

Another error source comes from the description of the transport of the particles through the spectrometer. In this case, the description was done with matrices with coefficients from the expansion of the transport equations in power series. The coefficients were calculated up to third order. The accuracy of this model is of about ∼1 %. Finally the total uncertainty of this calculation is estimated to be around 2 % [23].

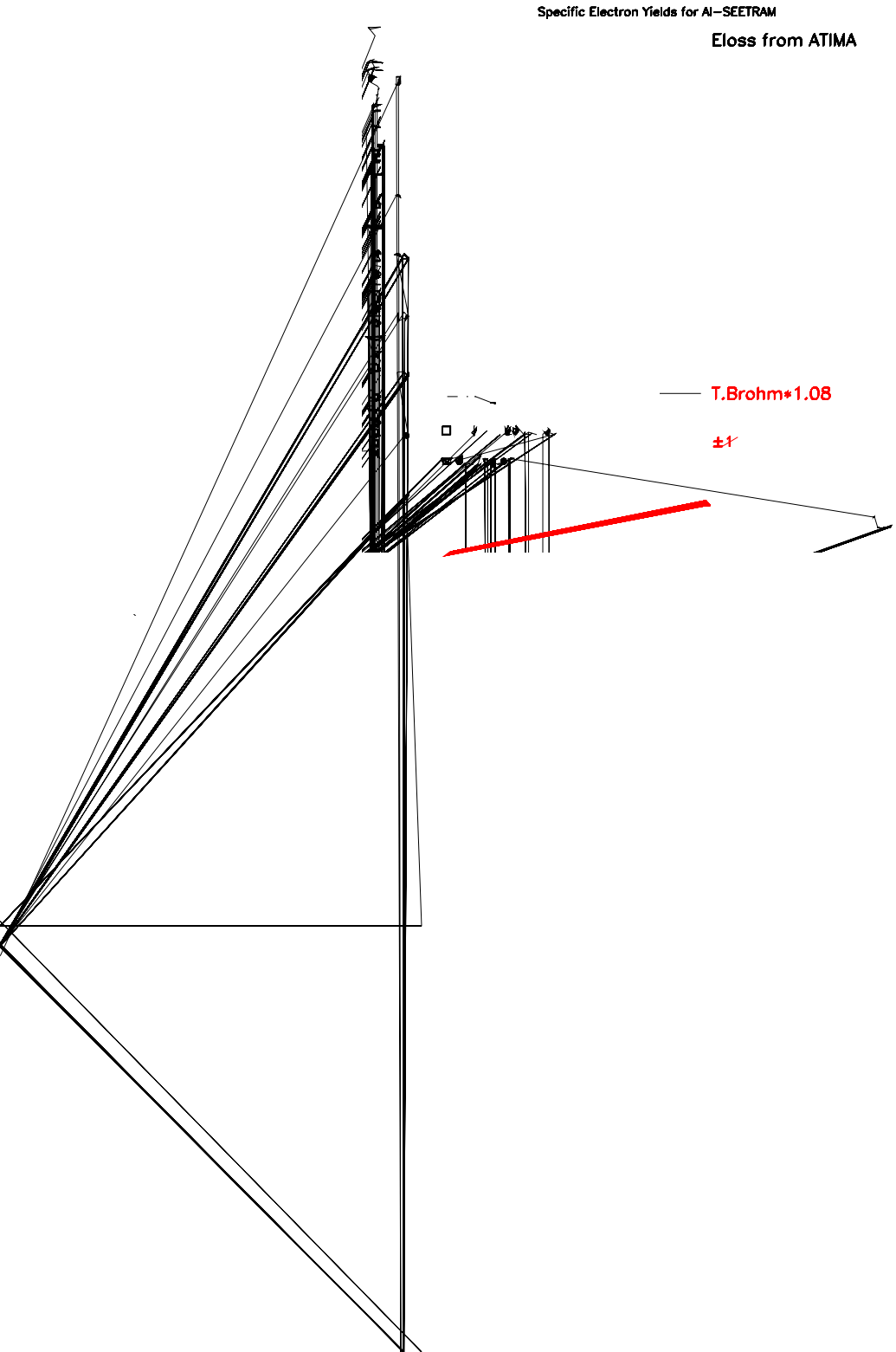
Specific Electron Yields for Al–SEETRAM
Eloss from ATIMA
T.Brohm*1.08
±1

Chapter 4

Results

In this work we have measured the production cross sections, σ_{prod}, of neutron deficient isotopes produced in the fragmentation reaction of ^{36}Ar projectiles with a ^{9}Be target, at 1050 A·MeV. We have been able to determine the production cross sections for 38 different isotopes from N to Ar, with an accuracy between 4 and 59 %. The results are presented in table 4.1 and plotted in fig. 4.2 with their corresponding uncertainties.

The measured data are compared in the following sections with three different codes: a semi-empirical formula, EPAX [6][7], and two theoretical models: the Abrasion-Ablation model, (*Abrabla* code) [3], and the intra nuclear cascade (*ISABEL* code) [4][5]. The data resulting from this work allow to test these models in the region of neutron-deficient nuclides, reaching the line of bounding nuclei, the so-called proton drip line. The models are briefly reviewed and the comparison is discussed in the next section.

In tables 4.2, and 4.3, the calculated width of the momentum distributions, and the parallel momentum transfer of all identified fragments are presented. These values for the momentum transfer, and width of these distributions are compared with the predictions of two well-known models. The theoretical formula given by Goldhaber [11], and the Morrissey semi-empirical approximation [10]. Since the fragmentation reaction of this experiment produces light nuclides, we cover a small range in $\Delta A = A_{projectile} - A_{fragment}$ but a wide one in $\Delta A / A_{projectile}$. In section 4.2 we give a short explanation about both models and the discussion of the comparison with the data.

$Isotope$	σ_{prod} (mb)	$Isotope$	σ_{prod} (mb)
^{12}N	0.092 ± 0.003	^{23}Al	0.016 ± 0.001
^{13}N	1.16 ± 0.37	^{23}Mg	3.48 ± 0.11
^{13}O	0.016 ± 0.001	^{24}Al	0.24 ± 0.01
^{14}O	0.16 ± 0.01	^{24}Si	$1.7 \cdot 10^{-3} \pm 1.0 \cdot 10^{-3}$
^{15}O	4.42 ± 0.14	^{25}Al	2.66 ± 0.39
^{16}O	17.7 ± 2.9	^{25}Si	0.027 ± 0.001
^{17}F	1.41 ± 0.05	^{26}Si	0.29 ± 0.01
^{17}Ne	0.011 ± 0.001	^{27}P	$6.5 \cdot 10^{-3} \pm 1.3 \cdot 10^{-3}$
^{18}F	7.01 ± 1.25	^{27}Si	5.09 ± 0.86
^{18}Ne	0.29 ± 0.01	^{28}P	0.20 ± 0.01
^{19}Ne	1.91 ± 0.06	^{29}P	2.44 ± 0.16
^{20}Mg	$1.5 \cdot 10^{-3} \pm 0.1 \cdot 10^{-3}$	^{29}S	0.028 ± 0.001
^{20}Na	0.29 ± 0.01	^{30}S	0.24 ± 0.01
^{20}Ne	10.8 ± 2.5	^{31}Cl	0.011 ± 0.003
^{21}Mg	0.019 ± 0.004	^{31}S	3.68 ± 0.35
^{21}Na	1.85 ± 0.26	^{32}Cl	0.39 ± 0.12
^{22}Al	$1.6 \cdot 10^{-3} \pm 0.2 \cdot 10^{-3}$	^{33}Ar	0.031 ± 0.001
^{22}Mg	0.34 ± 0.01	^{33}Cl	5.83 ± 1.66
^{22}Na	8.93 ± 2.79	^{34}Ar	0.50 ± 0.02

Table 4.1: *The final production cross sections in mb, with their corresponding uncertainties, for each studied isotope are displayed in this table.*

$Isotope$	$\sigma(P)$ $(MeVc)$	$Isotope$	$\sigma(P)$ $(MeVc)$	$Isotope$	$\sigma(P)$ $(MeVc)$
^{12}N	296.2 ± 2.4	^{20}Ne	301.5 ± 8.3	^{27}P	227.2 ± 3.7
^{13}N	322.3 ± 2.8	^{21}Mg	286.7 ± 8.3	^{27}Si	267.1 ± 2.7
^{13}O	280.5 ± 9.1	^{21}Na	272.8 ± 15.9	^{28}P	235.6 ± 2.5
^{14}O	298.8 ± 1.2	^{22}Al	290.0 ± 0.6	^{29}P	215.8 ± 2.0
^{15}O	288.7 ± 3.7	^{22}Mg	305.0 ± 3.6	^{29}S	232.5 ± 2.4
^{16}O	297.4 ± 15.9	^{22}Na	328.7 ± 9.6	^{30}S	204.8 ± 2.3
^{17}F	314.7 ± 4.3	^{23}Al	269.4 ± 5.6	^{31}Cl	164.5 ± 2.2
^{17}Ne	311.6 ± 3.4	^{23}Mg	306.3 ± 8.4	^{31}S	196.8 ± 6.6
^{18}F	288.0 ± 17.6	^{24}Al	292.5 ± 5.1	^{32}Cl	181.7 ± 3.3
^{18}Ne	312.0 ± 2.9	^{24}Si	276.6 ± 3.5	^{33}Ar	181.7 ± 3.5
^{19}Ne	286.2 ± 6.3	^{25}Al	286.3 ± 2.2	^{33}Cl	192.9 ± 1.5
^{20}Mg	264.5 ± 4.1	^{25}Si	270.3 ± 3.0	^{34}Ar	124.3 ± 2.7
^{20}Na	323.3 ± 3.7	^{26}Si	252.8 ± 2.2		

Table 4.2: *The table shows the measured value for the width of the momentum distributions for all the studied isotopes.*

$Isotope$	$< P'_{\parallel} > \ (MeVc)$	$Isotope$	$< P'_{\parallel} > \ (MeVc)$	$Isotope$	$< P'_{\parallel} > \ (MeVc)$
^{12}N	196.1 ± 112.6	^{20}Ne	287.1 ± 70.3	^{27}P	109.0 ± 40.4
^{13}N	194.3 ± 88.2	^{21}Mg	137.8 ± 65.7	^{27}Si	85.8 ± 53.7
^{13}O	167.9 ± 112.7	^{21}Na	188.6 ± 60.7	^{28}P	83.3 ± 39.5
^{14}O	141.7 ± 96.0	^{22}Al	160.3 ± 62.2	^{29}P	11.0 ± 40.4
^{15}O	161.3 ± 87.5	^{22}Mg	125.7 ± 67.6	^{29}S	75.3 ± 35.8
^{16}O	239.3 ± 58.2	^{22}Na	186.5 ± 59.0	^{30}S	71.5 ± 30.7
^{17}F	158.8 ± 80.0	^{23}Al	139.2 ± 53.7	^{31}Cl	68.2 ± 25.1
^{17}Ne	142.0 ± 88.8	^{23}Mg	114.9 ± 58.9	^{31}S	37.2 ± 32.1
^{18}F	150.1 ± 57.5	^{24}Al	99.0 ± 58.9	^{32}Cl	59.7 ± 26.4
^{18}Ne	149.0 ± 82.7	^{24}Si	84.6 ± 57.6	^{33}Ar	37.6 ± 22.4
^{19}Ne	169.7 ± 73.0	^{25}Al	120.5 ± 50.4	^{33}Cl	51.1 ± 17.5
^{20}Mg	185.1 ± 56.5	^{25}Si	110.4 ± 52.2	^{34}Ar	23.2 ± 16.0
^{20}Na	113.6 ± 75.0	^{26}Si	105.2 ± 44.4		

Table 4.3: *The table shows the measured value for parallel momentum transfer of the identified isotopes.*

4.1 Comparison of the experimental cross sections with model predictions

According to the two-step model proposed by Serber [24] in 1947, fragmentation reactions can be understood as a sequence of two different phases. In the first one, the projectile interacts with a nucleus at rest, losing part of its mass and momentum, and leading to a projectile residue in an excited state (prefragment). The second phase is considered as a statistical process in which the prefragment releases energy by emitting nucleons, pions and light nuclei until the final residue reaches its ground state.

Unlike the second phase, which is well described by the statistical model proposed by Weisskopf [25] and by Hauser [26], the first step is a much more complicated process still under discussion. Nowadays, many different approaches are used to describe this phase. The differences among these descriptions motivate the large amount of existing models.

When comparing theoretical predictions with data, these models are implemented by codes. In the present chapter we have compared our experimental data with results given by two different codes, namely ISABEL, based on the intra nuclear cascade model and Abrabla which implements the Abrasion model. Both codes use different approaches to describe the first step.

4.1.1 Comparison with the ISABEL code

In the intra nuclear cascade model the first step in the fragmentation reaction is described as a sequence of two body interactions among the nucleons of the projectile and the nucleons which constitute the target. The interacting particles (participants) are considered classically in the sense that their trajectories in the phase space are well defined at any time. The only quantum mechanical concept introduced in the model is the Pauli's principle. In addition, the sequence of interactions are determined randomly (Monte Carlo philosophy) within the probability distributions given by the nucleon-nucleon interaction cross sections.

The ISABEL code [4][5] considers the target nucleus as a degenerated Fermi gas which is well described by eight different regions of nuclear density. At the starting point the projectile interacts with this gas transferring part of its energy and moving one of its nucleons upward in energy. If this energy is above a certain threshold, then the trajectory of the excited nucleon is followed inside the nucleus. The probability of interaction among the excited particles with the Fermi gas is examined at each interval of time. As a consequence of these interactions the number of excited nucleons raises, thus leading to an intra nuclear cascade. The excited nucleons can also leave the nucleus. The process ends when the kinetic energy of all the participants is bellow a certain threshold, due to the interactions with the Fermi sea. Then, the whole nucleus is considered as a compound excited system which initiates the second step.

In figure 4.3 we compare the results given by this code (dashed lines) with our experimental measurements, represented by points.

The ISABEL code predictions are very close to the experimental data. The differences range between 20 % and 80 %, for isotopes lighter than Si. For heavier isotopes, from P to Ar, the predictions of ISABEL overestimate up to an order of magnitude the measured cross sections.

When the fragments come from mass losses larger than about 20 %, the isotope distributions are mainly dependent on the statistical evaporation from highly excited produced prefragments in the *limiting fragmentation* regime. The isotope distributions become almost independant on the original projectile-target combination, and their principal dependence are on their mass numbers. This region is the so-called *residue corridor*, showed for our experimental case in fig. 4.1.

ISABEL describes correctly the *limiting fragmentation* region but presents some disagreement to describe isotopes close to the projectile, where the influence of the entrance channel is important. This effect could be due to an underestimation

of the excitation energy of the prefragments just after the reaction, leading to a shorter evaporation, and increasing the production yield close to the projectile. The evaporation processes inside the residue corridor fit very well with our data.

In general ISABEL predictions fit well with our measurements with a small overestimation, but when we go up in charges higher than Z=14 ISABEL calculations separate from the experimental data, maybe due to an underestimation of the excitation energy in the produced prefragment.

4.1.2 Comparison with the Abrasion-Ablation Model

The abrasion model [27] considers two geometrically defined zones: an overlap "participator" zone where nucleons of projectile and target interact, and the non-overlapping "spectator" which defines the prefragment where part of the nucleons move almost undisturbed with their initial velocities. For a specific projectile-target configuration, the number of removed nucleons from the projectile and the target depends on the impact parameter, and it can be calculated by integration of the overlap volume. The excitation energy is given by the energy of the holes produced by the removed nucleons in their Fermi distribution inside the nucleus, and is estimated around 27 MeV per abraded nucleon. The second phase of the reaction is considered after the number of removed nucleons and the excitation energy are calculated, in the statistical evaporation code Abla [28].

The comparison of fig. 4.3 shows the validity of the Abrabla model [3] (dotted lines), since the model fits very well with the experimental data. The differences between the predictions of Abrabla and the data vary between 20 % and 100 % in most of the cases. There are points where the differences reach values bigger than 100 %, particularly in the case of ^{34}Ar, wich doubles the data; ^{31}Cl, with a factor 5, and ^{27}P with almost an order of magnitude. The two last cases correspond to points that are some of the "problematic" fits we mentioned in chapter 3.

In the case of the Ar isotope the discrepancy is not related with those problems in the data analysis. The discrepancy appears with the other Ar isotope too. Another case where we find a little discrepancy between predicted and measured data are the F isotopes. Here the model follows the behavior of the cross section, but the predicted values for the cross sections are slightly overestimated, up to a factor 2, compared with the measurements. In general, this overestimation appears in almost all the isotopes, like in the ISABEL code, with the exception of the O, where the prediction to the production cross section of ^{15}O is underestimated. The cause to this discrepancy may be the treatment of the total cross section, where some mechanisms can be overestimated. These similitudes between Abrabla and ISABEL disappear

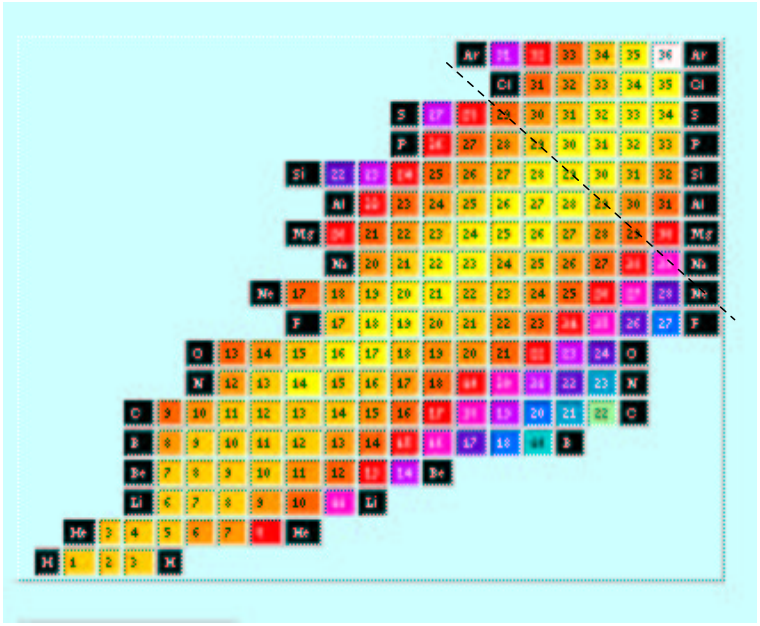

Figure 4.1: *The predicted data for our experiment by EPAX formula. The darker points corresponds to lower cross sections. An approximated limit to the residue corridor (cross sections independent from the original nucleus), is marked with a dashed line.*

when we look to charges higher than Z=14, where the ISABEL code predictions begin to separate from the other models compared.

In conclusion, the Abrabla model is the best of the two models, fitting so well with our results in all the identified species. The evaporation processes work nicely all along the residue corridor, the predictions for masses near to the projectile are so good, which point out a right estimation of the excitation energy inside the nucleus.

4.2 Comparison with EPAX

The semi-Empirical PArametrization of fragmentation X-sections,(*EPAX*), was proposed in 1990, by K. Sümmerer *et al.* [6], based on similar previous descriptions [29]. The description of high-energy fragmentation cross sections, σ_p, through the EPAX formula is valid only for the *limiting fragmentation* [8], where the σ_p becomes energy independent. This regime is experimentally reached when incident energies are considerably above the Fermi energy of the nuclei ($\sim$40 A·MeV). EPAX predictions have no dependence on energy.

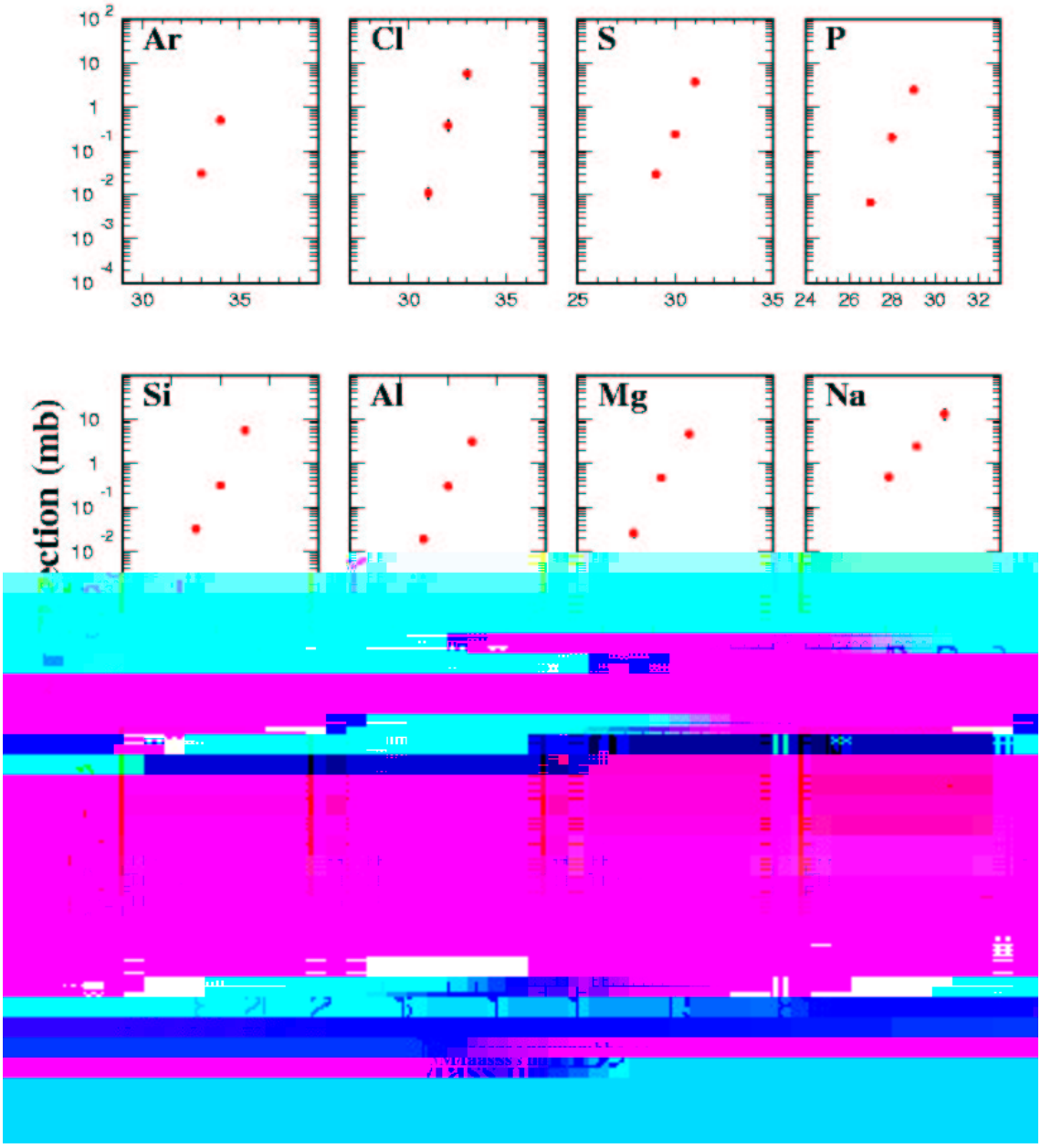

Figure 4.2: *The figure shows the production cross sections for all the measured fragments in the experiment.*

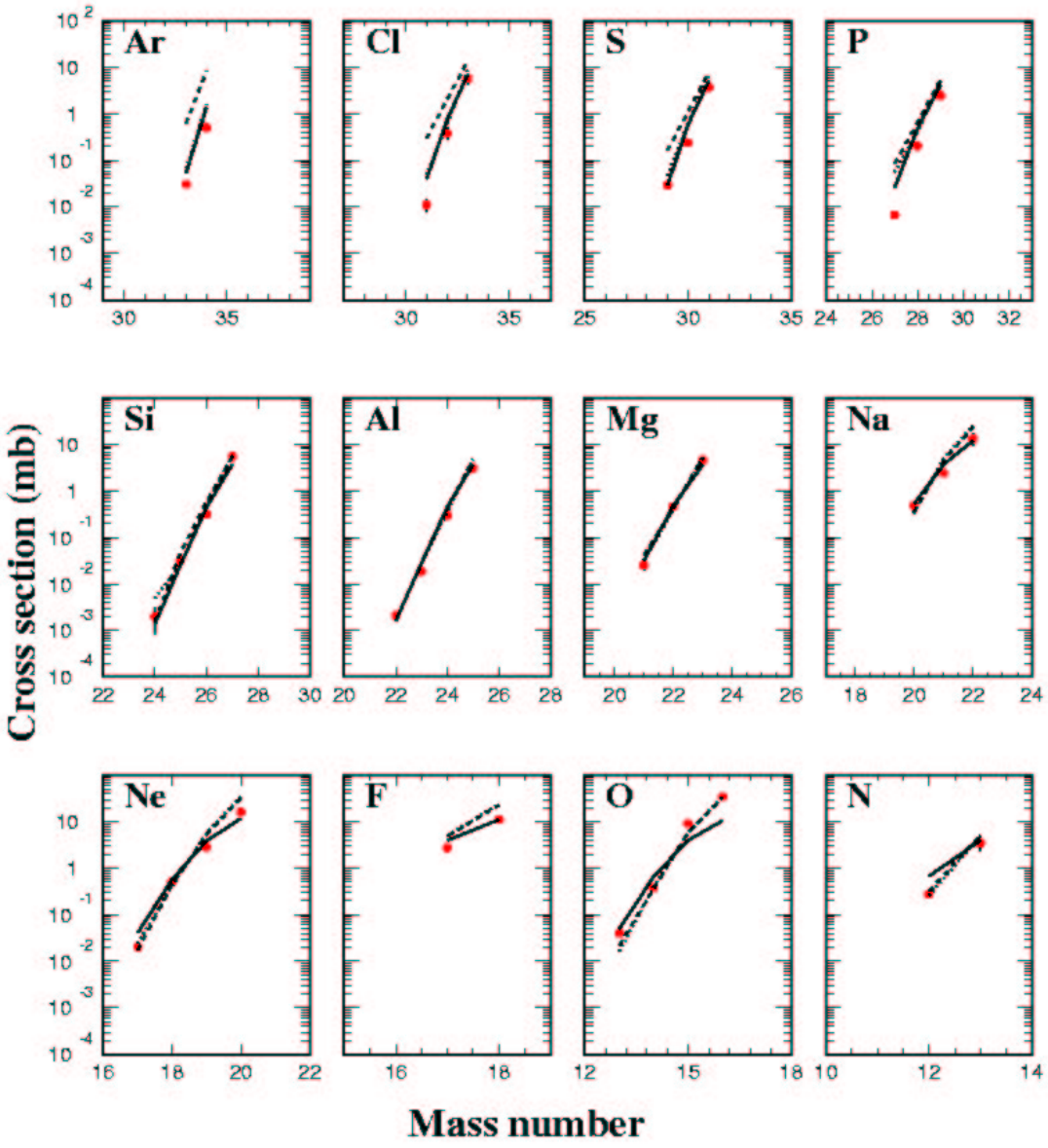

Figure 4.3: *The figure shows the production cross sections for all the measured fragments in the experiment (points), compared with the predictions of EPAX formula (solid line), the ISABEL code (dashed line), and the Abrasion-Ablation model (dotted line).*

EPAX describes the fragmentation of medium-to heavy-mass projectiles. Nucleon-pickup or fragmentation of fissile nuclei are not included. The range of validity for this formula extends from Ar, up to Pb and Bi isotopes. In this work we test EPAX in its lower mass extreme.

The figure 4.3 shows the graphical comparison between the measured data (points) and the predictions of the EPAX formula (solid lines). We observe a good agreement between the experimental results and the EPAX predictions comparable with the two models described before, with differences that range between 10 % and a factor 3. The biggest differences correspond to some of those points that we found "problematic" in the data analysis. EPAX predictions do not show a general trend to over or underestimations in any specie. We can point out that overestimations seem to appear for lower masses, while a smooth tendency to underestimate appears for higher isotope masses, in our data. This behavior is clear in the case of O and Ne isotopes. The authors of the EPAX formula give limits of validity for this formula, that in the case of our experiment, corresponds to Ne isotopes. With lower charges the data reproduction is not guarantee, but, even for those cases, the predictions are quite good. Our measured data may help to improve the EPAX formula, and extends its range of validity.

Finally we can observe in the comparisons that the best predictions for the three models correspond to intermediate masses. For these isotopes, (Si, Al, Mg, and Na), the three models are coincident in their predictions. Then, for higher masses the production cross sections of ISABEL overestimate, maybe due to a wrong estimation of the excitation energy, and for lower masses the behavior of EPAX formula is slightly different from the other two models, due to its inherent limit of validity.

4.3 Comparison of the measured momenta with Morrissey and Goldhaber Models

The study of a reaction can be done through its kinematics, in particular, the momentum distribution of the produced fragments helps to understand the process of fragmentation. We have measured the momentum distribution for all the fragments studied in our experiment, see fig. 4.5. We compare, in this section, our experimental results with predictions of two different models, the Goldhaber model [11], and the semi-empirical parametrization of Morrissey [10].

The width of the momentum distribution is a useful observable to test the validity of such models. The Goldhaber model predicts a simple relation between the

momentum width and the masses of the projectile and the fragment:

$$\sigma(P_{\|})^2 = \sigma_0^2 \frac{A_f(A_p - A_f)}{(A_p - 1)} \tag{4.1}$$

where A_f is the mass of the fragment, and A_p the mass of the projectile, and σ_0 ≈90 Mev/c, as an experimental approach to the Fermi momentum, $\sigma_0 \propto p_F$. To obtain this relation different assumptions on the mechanisms of the fragmentation process are necessary. This model concludes that the momentum distribution of the produced fragments is not sensitive to the velocity of the fragmentation, and cannot describe the fragmentation process.

In the Morrissey approximation, evaporation processes are included taking into account not only theoretical considerations but different fragmentation data to improve its predictions. The description for the momentum of the fragmentation residues can be done by a simple dependence on the mass loss through:

$$\sigma(P_{\|}) = \frac{150}{\sqrt{3}} \sqrt{A_p - A_f} \tag{4.2}$$

Morrissey compared the predictions of the formula with statistical evaporation calculations and showed that part of the isotropic momentum is produced in the initial stage of the collision. Individual contributions of the involved processes in the fragmentation can not be identified, due to their similar dependence on the difference between projectile and fragment masses.

The measured momentum distribution widths of the produced fragments presented in the fig. 4.4 show a good agreement with both Goldhaber and Morrissey predictions, up to a mass loss of ∼14, that is ∼40 % of the initial mass. This limit can be found in other works, i.e.: the results of M. Weber et al [31], for 500 A·MeV ^{86}Kr+^{9}Be.

We observe an overestimation in the Goldhaber predictions, that can be attributed to evaporation process, which contributes to decrease the mass, and this is not taken into account. For high mass losses our data follow Goldhaber and deviate from Morrissey predictions. This behavior may indicate that these fragments come from central collisions followed by multi fragmentation, not from peripheral ones as those associated with a small mass losses. The Goldhaber model fits better in our situation, while Morrissey calculations seems to be better for higher projectile masses, where evaporation process is more relevant. Even more, in the Morrissey predictions the momentum distribution depends only on the mass loss, while the Goldhaber formula uses the ratio between the mass loss and the initial mass. The Goldhaber formula seems to be more sensitive to the initial conditions of the experiment.

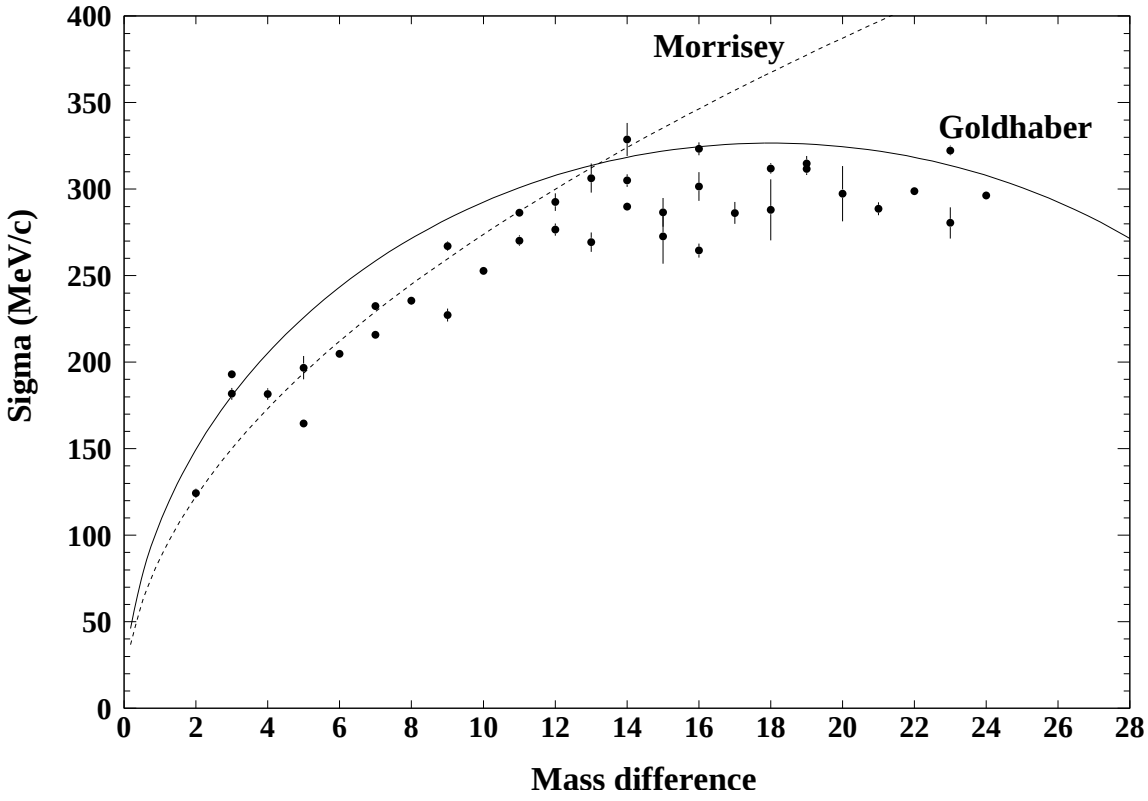

Figure 4.4: *The momentum distribution with is represented in this figure versus the difference between projectile and fragment masses. The points correspond to experimental measurements, the dashed line follows the Morrissey predictions, and the solid line represents the Goldhaber calculations.*

Morrissey describes the momenta of the primary residues in fragmentation assuming that $\Delta m/m_{targ}$ is small. Following this assumption the momentum of the fragments can be written as: $q \approx m_{proj} < \beta_{||} >$. In this scenario the average parallel momentum transfer of the products is defined as a product of the measured velocity of the fragment, $< \beta_{||} >$, the projectile mass, m_{proj}, and a kinematic factor, $\beta\gamma/(\gamma+1)$:

$$< P'_{||} > \equiv m_{proj} < \beta_{||} > \beta\gamma/(\gamma+1) \tag{4.3}$$

Morrissey found a systematic between the parallel momentum transfer, $< P'_{||} >$, and the mass difference, ΔA. This systematic was established from the analisys of fragments coming from fragmentation of different projectiles rangin from ^{40}Ar to ^{197}Au (see reference [10] for further details). This systematic is translated in a linear relation: $< P'_{||} > \propto \Delta A$ with a fitted slope of 8 MeV/u [10].

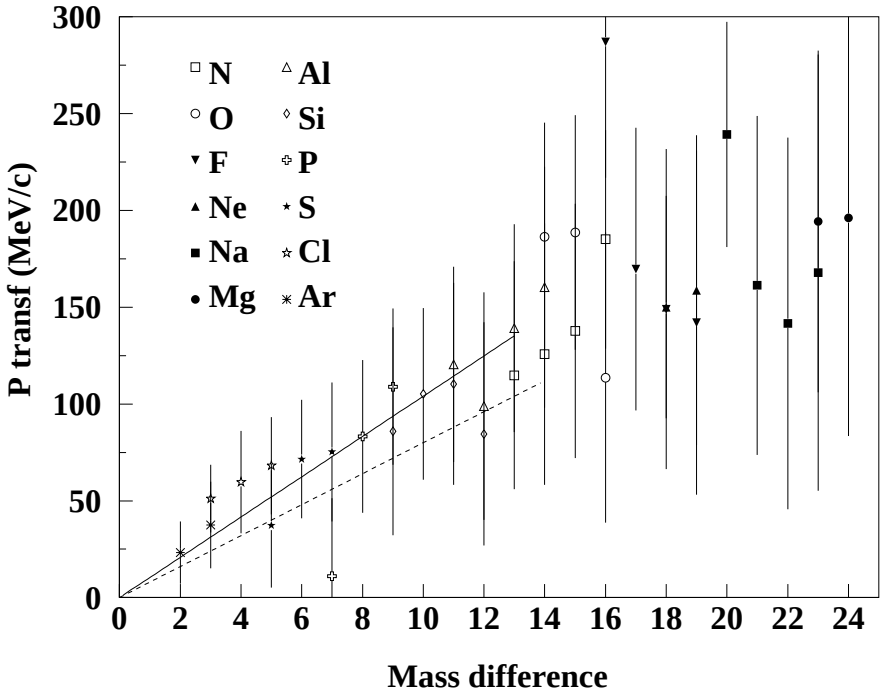

Figure 4.5: *The average parallel momentum transfer versus the difference between projectile and fragment masses is plotted in the figure. The solid line correspond to the 10.4 MeV/u fit of the data. The dashed line is the 8 MeV/u fitted slope found by Morrissey* [10].

In order to compare our data with these results we calculate the velocity of each fragment from the measurement of its magnetic rigidity, and we correct it from the energy losses in each slice of matter in the fragments' path. The data are translated to the projectile frame and multiplied by the kinematic factor. The results of these calculations are summarized in table 4.3, and plotted in fig. 4.5 versus the mass loss, ΔA. The fit of these data yields a slope of 10.4 MeV/u. The performed fit was done in the region where a linear relation is, more or less, observable. The assumptions of Morrissey are established for a mass loss approximately equal to the target (ΔA $\sim$9, in our case). We, however, extend this region up to ΔA=13, where we consider that reactions different from spallation start to contribute. A mass loss larger than 14, that is $\sim$40 % of the projectile mass, involves more central collisions, and the assumptions about the reaction mechanism begin to fail, as in the

previous discussion about the momentum width. This kind of systematic behavior was already observed in other works. We just mentioned the results of M. Weber et al [31], where the authors fitted a slope of 8.8 MeV/c, for 500 A·MeV ^{86}Kr+^{9}Be.

Chapter 5

Conclusions

We measure in this work the production cross sections, σ_{pro}, for 39 different fragments from ^{36}Ar + ^{9}Be projectile fragmentation at 1050 A·Mev. The experiment was done in the FRS [9] spectrometer, at GSI. The studied fragments cover a mass region from A_f=12 up to A_f=35, with isotopes from N up to Ar. Systematic measurements with different magnetic settings in the spectrometer allow to reach the proton drip line for N, O, F, Ne, Na, Mg, Al, and Cl.

The σ_{pro} are obtained by integration of the Bρ distributions for each isotope. The different magnetic settings allow to reconstruct the Bρ distributions along the range of magnetic rigidity covered by the settings. This range runs from 9.11 Tm up to 10.92 Tm, where the proton drip line is reached. The resulting yields are normalized to the number of atoms in the target, and to the number of projectiles in the incident beam. The number of particles in the beam was measured with the SEETRAM [15] monitor, calibrated in this work. We measure cross sections from $\sim$10 μb up to $\sim$10 mb.

The obtained data may help to plan new experiments involving the exotic nuclides identified. The measurements of the production cross sections help to develope secondary beams with neutron-deficient species.

The measured cross sections are compared with three models: the semi-Empirical PArameterization of fragmentation cross sections, (*EPAX*) [6][7], the ISABEL [4][5] and the Abrabla codes [3]. The EPAX formula is tested in one of its validity limits, light neutron-deficient nuclides around Ar. The three models fit nicely with our results, they disagree only in a few regions. In the case of the intranuclear cascade model, ISABEL, its predictions are slightly higher than our data, but they do not separate more than a 100 % in the lower and middle charges. For higher charges,

more than Z=14, ISABEL overestimate the data up to an order of magnitude. This disagreement can be due to a subestimation of the excitation energy in the first stage of the reaction. This subestimation leads to less evaporation processes, and higher yields and cross sections, close to the projectile. In the residue corridor, where the excitation energy is no longer important, ISABEL fits quite well with our data.

The other theoretical model compared, the Abrasion-Ablation model, exceedes in its predictions too, but never more than a factor 2, except in some cases belonging to those where estimations in the analysis are needed. The predictions close to the projectile fit well to our results, this may indicates a good estimation of the excitation energy. The process estimations in the residue corridor are nearly equal to the ISABEL one, and very close to our data. The Abrasion-Ablation model gives, in general, the best fit of the three models, for all the identified species.

EPAX coincides with the measured data with differences near to those of Abrabla and ISABEL codes, except for lower charges, less than Z=10, where the predictions are overestimated for lower masses and underestimated for higher masses of each isotope. This effect is due to the EPAX limit of validity, that in our case, are the Ne isotopes. The measured data may help to improve the predictions of EPAX, and extends the region of validity up to lower masses.

The measurement of momentum distributions is also done for the produced fragments. The Bρ distributions are translated to momentum distributions and then fitted, in order to get the mean value, and the width of the momentum distributions.

The results of the calculation of velocity are translated to parallel momentum transfer, in order to compared with the predictions of Morrissey [10]. In this model a relation of the momentum transfer with the mass loss is predicted, and fixed in a slope of 8 MeV/u. We observe a systematic behavior which can be read as a proportional relation between the momentum transfer and the mass loss, with a slope of 10.4 MeV/u. We also reach the point where the asumptions and conclusions of Morrissey are no longer valid due to a high mass difference between the projectile and the fragment.

The calculation of the width of the momentum distributions allows to check the validity for two different approaches to the momentum distributions in fragmentation process: the Goldhaber formula [11], and the semi-empirical Morrissey model [10]. The measured data show a good agreement with the Goldhaber formula, while the Morrissey predictions deviate from both experimental results and Goldhaber calculations. The Morrissey model takes into account evaporation processes, but these are only relevant for higher masses. The Goldhaber model is more sensitive to the mass of the projectile, and this sensitivity leads to a better fit for low projectile masses.

Chapter 6

Resumen

Desde los pioneros experimentos en Berkeley [1][2], la fragmentación en vuelo ha sido muy usada para producir isótopos radioactivos lejos de la estabilidad. La reciente producción de haces secundarios ha ensanchado el campo de estudios de la física nuclear haciendo posible experimentos con especies exóticas. La medida de secciones eficaces de producción figura entre los primeros experimentos hechos con estos haces secundarios. Este tipo de experimentos dará información importante para planificar otros experimentos con haces exóticos (estimaciones de tiempo de medida), a la vez que pueden ser utilizados para extraer información acerca de los mecanismos de reacción.

La sección eficaz de producción (σ_{pro}) es la probabilidad de producir cierto isótopo en una cierta reacción por unidad de área. Experimentalmente puede ser definida como el número de partículas producidas (N_p) dividido por el número de partículas incidentes (N_i) y el número de atomos en el blanco por unidad de área (T_f):

$$\sigma_{pro} = \frac{N_p}{N_i \cdot T_f} \; barns \tag{6.1}$$

La mejor situación correspondería al caso donde todas las secciones eficaces de producción pudiesen medirse en el laboratorio. Esta situación no es realista debido al gran número de isótopos exóticos que pueden ser producidos. De todas formas es importante realizar estas medidas a lo largo de la carta de núcleos para construir una base de datos que pueda ser usada para la optimización de modelos teóricos que predigan estas cantidades. El principal obstáculo de estos modelos es que los cálculos que precisan requieren mucho tiempo. Bajo esta perspectiva es importante desarrollar parametrizaciones capaces de estimar estas cantidades.

Las secciones eficaces de producción son difíciles de predecir con los modelos actuales de fragmentación, como el Abrasion-Ablation model (Abrabla) [3] o el modelo de cascada intranuclear (ISABEL) [4][5]. De todas formas, existen otras formas de acercarse a estos resultados. Usando una parametrización empírica uno puede estar seguro que sus predicciones están cerca de los resultados experimentales, ya que están basadas en datos empíricos. Su grado de precisión depende de la calidad y cantidad de datos tenidos en cuenta. Una de estas aproximaciones es la llamada fórmula EPAX [6][7].

En este trabajo hemos medido la sección eficaz de producción para 39 fragmentos diferentes de la reacción de fragmentación de ^{36}Ar + ^{9}Be a 1050 A·MeV. El experimento fue hecho en el espectrómetro FRS, en el GSI. Los fragmentos estudiados cubren una región en masa desde A_f=12 hasta A_f=35, con isótopos desde N hasta Ar. Medidas sistemáticas con diferentes campos magnéticos en el espectrómetro permiten llegar al límite de ligadura de protones para N, O, F, Ne, Na, Mg, Al, y Cl.

Las secciones eficaces son calculadas integrando las distribuciones de rigidez magnética para cada isótopo. Los diferentes valores en los campos magnéticos permiten reconstruir las distribuciones de rigidez magnética a lo largo de la región cubierta por los imanes. Este rango va desde 9.11 Tm hasta 10.92 Tm, donde se alcanza el límite de ligadura de protones. Las integrales resultantes son normalizadas por el número de atomos en el blanco, y el número de proyectiles en el haz incidente. El número de partículas en el haz fue medido con el monitor de haz SEETRAM, calibrado en este trabajo. Medimos secciones eficaces de unas decenas de μb hasta decenas de mb.

Los datos obtenidos pueden ayudar a planear experimentos en los cuales participaran núcleos exóticos como los que hemos identificado en este trabajo. La medida de nuestras secciones eficaces ayuda a desarrollar haces secundarios con especies deficitarias en neutrones, haciendo más accesibles estas zonas de estudio, cerca del límite de ligadura de protones.

Las secciones eficaces calculadas son comparadas con tres modelos: el modelo semiempírico EPAX, y los modelos teóricos de cascada intranuclear (ISABEL), y el modelo de abrasión (Abrabla). La fórmula EPAX es probada en uno de sus límites de validez, los núcleos ligeros deficitarios en neutrones alrededor del Ar. Los tres modelos estan en buen acuerdo con nuestros resultados, encontrando diferencias sólo en regiones muy localizadas. En el caso del modelo de cascada intranuclear ISABEL, las predicciones son ligeramente superiores a los datos medidos, pero no se alejan más allá de un 100 % del valor experimental en las cargas ligeras e intermedias. Para las cargas mas altas, a partir del P, ISABEL sobreestima los datos hasta en un orden de magnitud. Esta diferencia puede ser debida a una subestimación de la energía

de excitación en la reacción. Esta subestimación lleva a una menor evaporación justo después de la reacción, y a mayores secciones eficaces cerca del proyectil. En el corredor de residuos, dónde la energía de excitación no es importante, ISABEL encaja muy bien con nuestros datos.

El otro modelo teórico comparado, el modelo de Abrasión-Ablación, también se excede en sus predicciones, pero nunca más allá de un factor 2, excepto en algunos casos pertenecientes a aquellos problemáticos en su análisis. Las predicciones cerca del proyectil dan un buen ajuste con nuestros resultados, esto puede indicar una correcta estimación de la energía de excitación. Los procesos en el corredor son prácticamente iguales a los de ISABEL, y muy cercanos a nuestros datos. El modelo Abrabla da, en general, el mejor ajuste de los tres modelos en todas las especies identificadas.

EPAX, por su parte, coincide con los datos medidos con diferencias cercanas a las de Abrabla, salvo para las cargas más bajas, a partir del Ne, en las que su comportamiento oscila en torno a los datos experimentales, con predicciones sobreestimadas en las masas más ligeras, y subestimadas para las masas altas de cada isótopo. Este efecto es debido al límite de validez de EPAX, que, en nuestro caso, son los isótopos alrededor del Ne. Los datos medidos pueden ayudar a mejorar las predicciones de EPAX, y extender su región de validez hasta masas más bajas.

En conclusión, las predicciones más estables son las dadas por Abrabla, mientras que ISABEL se aleja en las cargas altas, debido a una subestimación de la energía de excitación, y EPAX oscila en las cargas bajas que exceden su límite de validez.

La medida de las distribuciones de momento se han hecho también para los fragmentos producidos. Las distribuciones de rigidez magnética son traducidas a momento y luego ajustadas, para obtener su valor medio y la anchura de las distribuciones de momento.

Los resultados del cálculo de la velocidad son traducidos a momento paralelo transferido, para compararlo con las predicciones de Morrissey [10]. En este modelo se predice una relación entre el momento transferido y la pérdida de masa, y se fija una proporcionalidad de 8 MeV/u. Observamos un comportamiento sistemático que puede ser interpretado como una relación proporcional entre el momento transferido y la pérdida de masa, con una pendiente de 10.4 MeV/u. También llegamos al punto en el que las suposiciones y conclusiones de Morrissey ya no son válidas debido a una gran diferencia entre las masas del proyectil y el fragmento.

El cálculo de las anchuras de las distribuciones de momento permite probar la validez de dos diferentes intentos de describir las distribuciones de momento en procesos de fragmentación: la fórmula de Goldhaber [11], y el modelo semiempírico

de Morrissey [10]. Los datos medidos muestran un gran acuerdo con la fórmula de Goldhaber, mientras que las predicciones de Morrissey se separan de ambos resultados, el experimental y el de Goldhaber. El modelo de Morrissey toma en consideración procesos de evaporación, pero éstos son más relevantes con masas mayores. El modelo de Goldhaber resulta más sensible a la masa del proyectil, y esta sensibilidad lleva a un mejor ajuste para masas más pequeñas.

Bibliography

[1] D.E. Greiner et al., *Phys. Rev. Lett.* **35** (1975) 152.

[2] T.J.M. Symons et al., *Phys. Rev. Lett.* **42** (1979) 40.

[3] J.-J. Gaimard, K.-H. Schmidt, *Nucl. Phys.* A **531** (1975) 709.

[4] K. Chen et al., *Phys. Rev.* **166** (1969) 949.

[5] Y. Yariv et al., *Phys. Rev.* C **20** (1979) 2227.

[6] K. Sümmerer et al., *Phys. Rev.* C **42** (1990) 2546.

[7] K. Sümmerer, B. Blank, *Phys. Rev.* C **61** (2000) 034607.

[8] J. Benecke et al., *Phys. Rev.* **188** (1969) 2159.

[9] H. Geissel et al., *Nucl. Instrum. Methods* B **70** (1992) 286.

[10] D.J. Morrisey, *Phys. Rev.* C **39** (1989) 460.

[11] A.S. Goldhaber, *Phys. Lett.* B **53** (1974) 244.

[12] R. Bennett et al., *Radioactive Nuclear Beam Facilities* NuPECC Report (April 2000) 31.

[13] P. J. Lindstrom et al., *Lawrence Berkeley Lab. Rep.* LBL-3650 (1975)

[14] I. Tanihata, *Experimental techniques in nuclear physics* ed. D.N. Poenaru, W. Greiner **W. de Gruyter** (1997) Production and use of radioactive beams 357.

[15] C. Ziegler et al., *GSI Scientific Report* 1990, 1991, p. 291.

[16] V. Hlinka et al., *Nucl. Instrum. Methods* A **419** (1998) 503.

[17] M. Pfützner et al., *Nucl. Instrum. Methods* B **86** (1994) 213.

[18] R. Holzman et al., *GSI Scientific Report* (1992) 48.

[19] B. Voss et al., *Nucl. Instrum. Methods* A **364** (1995) 150.

[20] B. Jurado et al., *Nucl. Instrum. Methods* A **483** (2002) 603.

[21] http://www-wnt.gsi.de/kschmidt/seetraminfo/SEETRAM.html

[22] J. Benlliure, J. Pereira-Conca, K.-H. Schmidt. *Nucl. Instrum. Methods* A **478** (2002) 493.

[23] J. Pereira-Conca, *New Approach to evaluate the angular transmission of the in-flight separator FRS at GSI* Diploma thesis (2000)

[24] R. Serber, *Phys. Rev.* **72** (1975) 108.

[25] V. F. Weisskopf, D. H. Ewing, *Phys. Rev.* **57** (1940) 472.

[26] W. Hauser, H. Feshbach, *Phys. Rev.* **87** (1952) 366.

[27] D. J. Morrissey et al., *Phys. Rev.* C **18** (1978) 1267.

[28] A. R. Junghans et al., *Nucl. Phys.* A **629** (1998) 635.

[29] G. Rudstam, *Z. Naturforsch.* A **21** (1966) 1027.

[30] T. Brohm, www-wnt.gsi.de/Kschmidt/seetram.htm. 1994. Private communication from K. Sümmerer.

[31] m. Weber et al., *Nucl. Phys.* A **578** (1994) 659.